

# Possible quasi-periodic ejections in quasar B1308+326

S. J. Qian<sup>1,2</sup>, S. Britzen<sup>1</sup>, A. Witzel<sup>1</sup>, T. P. Krichbaum<sup>1</sup>, and H. Q. Gan<sup>1,2</sup>

<sup>1</sup> Max-Planck Institut für Radioastronomie, Auf dem Hügel 69, 53121 Bonn, Germany

<sup>2</sup> National Astronomical Observatories, Chinese Academy of Sciences, 100012 Beijing, PR China  
e-mail: rqsj@bao.ac.cn

Received 30 December 2016 / Accepted 19 May 2017

## ABSTRACT

**Context.** The search for periodic features in flux variability and kinematics of superluminal components in blazars is capable of providing significant clues for the understanding of the physical processes in their central engines (black-hole/accretion-disk systems), especially concerning the formation and structure of their relativistic jets and radiation mechanisms.

**Aims.** The jet swing on parsec-scales and the change of the ejection position angle of the superluminal components with time in the quasar B1308+326 ( $z = 0.997$ ) are investigated as quasi-periodic behaviors.

**Methods.** A previously published precessing jet nozzle model is applied to model the source kinematics and a possible jet precession period is found.

**Results.** Based on the model fitting of the kinematics for a subset of components, it is shown that their kinematics, including the shape of the inner trajectories and the motion of the components, could be well fitted in terms of the precessing jet nozzle model and a precession period of  $\sim 16.9 \pm 0.3$  yr is derived. Different precession mechanisms are discussed and compared.

**Conclusions.** It is shown that the swing of the ejection position angle of the superluminal knots observed in B1308+326 may be due to the orbital motion of a putative supermassive black hole binary in its nucleus. Some relevant parameters of the binary model are estimated. We also discuss the spin-induced precession mechanism in the single black hole scenario and an estimate for the spin of the Kerr black hole is obtained.

**Key words.** galaxies: active – galaxies: jets – galaxies: nuclei

## 1. Introduction

Blazars are objects characterized by extreme emission variability at all wavelengths from radio to  $\gamma$ -ray regimes. The strong variations in their radiation (flux and polarization) and the superluminal motion observed on pc-scales with very long baseline interferometry (VLBI) are largely related to the relativistic jets closely directed toward us. The search for periodic features in flux density and ejection of superluminal components on parsec-scales in blazars may provide significant clues for the understanding of the physical processes occurring in their central engines (supermassive-rotating-black-hole/accretion-disk systems), especially concerning the formation and energetics of the relativistic jets and their radiation mechanisms. There is growing evidence that a number of blazars display periodic behavior on timescales of years and decades. Observational evidence largely comes from two types of observations: Periodicities in optical and radio light curves, which are correlated in some cases, and periodic variations in the (compact) radio cores mapped by VLBI, which consist of the quasi-periodic undulating jet structures (swing of jet spines) and quasi-periodic wobbling of the ejection position angle of superluminal components. There have been many publications concerning several blazars, for example, 3C 273 (Abraham & Romero 1999; Savolainen et al. 2006; Calzadilla et al. 2015); BL Lacertae (Raiteri et al. 2001; Stirling et al. 2003; Tateyama 2009); PKS 0420-014 (Britzen et al. 2001); 3C 345 (Qian et al. 1991, 2009; Steffen et al. 1995); 3C 454.3 (Qian et al. 2007, 2014); 3C 279 (Qian 2012, 2013); NRAO 150 (Agudo et al. 2007; Agudo 2009; Molina et al. 2014; Qian 2016); B0605-085 (Kudryavtseva et al. 2011); B1308-326 (Lister et al. 2013; Britzen et al. 2017); OJ287 (Kikuchi et al. 1988; Vicente et al. 1996; Villata et al. 1998; Tateyama & Kingham 2004; Valtonen & Pihajok 2013); PG 1302-102 (Graham et al. 2015; Qian et al., in prep.). Calzadilla et al. (2015) recently reported

the detection of the jet precession on sub-parsec scales in the archetypal blazar 3C 273 with the Event Horizon Telescope at 1.3 mm wavelength.

These periodic (or quasi-periodic) variations are particularly important because they can put useful constraints on the structure and kinematics (even the formation) of the jets and on the emission mechanisms. Precessing relativistic beams have been invoked to explain these periodic phenomena while binary black hole systems and Lense-Thirring effect of Kerr (rotating) black holes have been applied to induce the precession of jets.

B1308+326 is a low-synchrotron-peaked high polarization quasar, showing a core-jet structure with prominent apparent superluminal motion. Recently, Britzen et al. (2017, hereafter BQS17) re-modeled VLBA (Very Long Baseline Array) observations (at 15 GHz) from the MOJAVE (Monitoring Of Jets in Active galactic nuclei with VLBA Experiments) survey with Gaussian components within the *difmap*-modelfit programme (Shepherd 1997) and found that its jet features (knots)<sup>1</sup> are emitted with varying position angles within an ejection cone. In this paper we perform a detailed analysis and model fitting of the source kinematics and show that the swing of the inner jet position angle of the superluminal components could be interpreted in terms of the precessing jet nozzle model proposed by Qian et al. (1991, 2009, 2014) with a precession period of  $\sim 16.9 \pm 0.3$  yr.

## 2. Geometry of the model

In order to perform model fitting of the VLBI-kinematics of the quasar B1308+326 in terms of a precessing nozzle model, we

<sup>1</sup> Superluminal components (or knots) in jets are usually referred to as inhomogeneities in the jet brightness distribution formed from shocks (Marscher & Gear 1985).

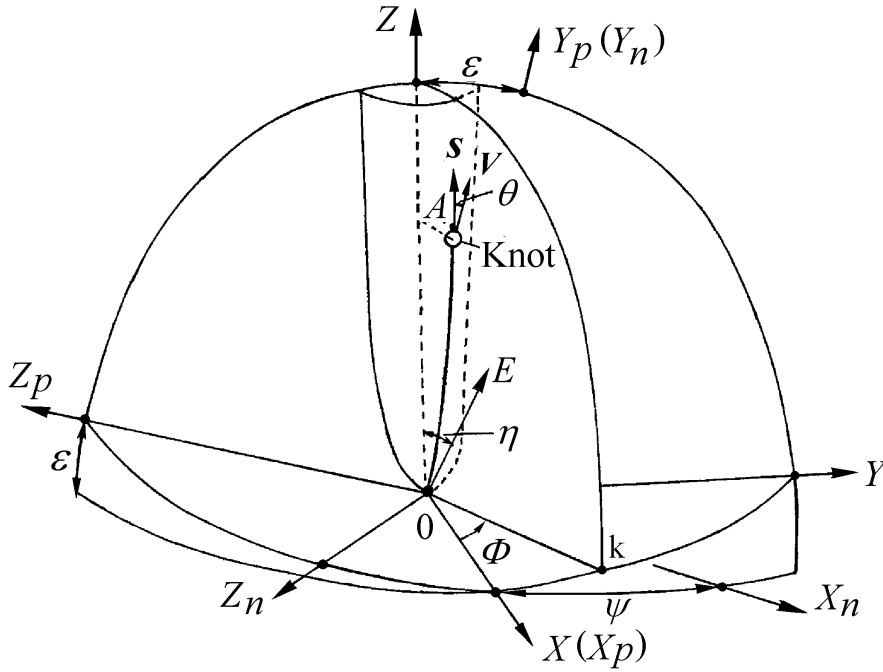


**Fig. 1.** Geometry of the precession model (not to scale) adopted from Qian (2011). The  $Z$ -axis, which is taken to be the axis of precession, is defined by parameters  $(\epsilon, \psi)$ ; the  $Y_p$  axis indicates the direction toward the observer; the position of a knot (superluminal component) is defined by parameters  $(A, \Phi)$ ;  $A(Z)$  is the amplitude function and  $\Phi$  is the azimuthal angle (or phase); the plane  $(X_p, Z_p)$  represents the plane of the sky; and  $\theta$  denotes the angle between the knot's velocity vector ( $S$ ) and the direction toward the observer ( $V$ ).  $\eta$  is the initial half opening angle of the precessing jet cone (see text).

first give the description of the formalism of the model. Following Qian et al. (1991, 2009, 2014), we take the geometry of the model as shown in Fig. 1, in which the coordinate system  $(X_p, Y_p, Z_p)$  has the  $Y_p$ -axis directed toward the observer, that is, the plane  $(X_p, Z_p)$  is defined as the sky plane. In this plane the  $Z_n$ -axis is defined as the direction toward the north pole and the  $X_n$ -axis as opposite to the direction of right ascension. The observed position angle of VLBI knots is measured clockwise from the  $Z_n$ -axis. We define a third coordinate system  $(X, Y, Z)$ : The  $X$ -axis coincides with the axis  $X_p$  and the  $Z$ -axis is situated in the  $Y_p$ - $Z_p$  plane forming an angle  $\epsilon$  with the  $Y_p$ -axis. The  $Z$ -axis is defined as the jet-axis around which the precessing nozzle rotates.  $\psi$  denotes the angle between the  $X(X_p)$ -axis and the  $X_n$ -axis. The precession cone has an initial half opening angle of  $\eta$ .

We assume that the superluminal knots move along individual collimated trajectories, as shown in Fig. 1. Each of the VLBI knots moves along a curved trajectory with a constant phase  $\Phi$ , but for the successive knots the phase changes due to precession. The trajectory of a knot is defined by its amplitude function  $A(Z)$  and phase  $\Phi$ . In Fig. 1,  $S$  denotes the direction of the spatial velocity and  $V$  denotes the direction toward the observer (parallel to the direction  $Y_p$ ).  $\theta$  denotes the viewing angle of the knot's motion.

Thus, the trajectory of a knot can be described in the  $(X, Y, Z)$  system as follows.

$$X(Z, \Phi) = A(Z)\cos \Phi, \quad (1)$$

$$Y(Z, \Phi) = A(Z)\sin \Phi. \quad (2)$$

The projection of the trajectory on the sky plane is represented by

$$X_n(Z, \Phi) = X_p(Z, \Phi)\cos \psi - Z_p(Z, \Phi)\sin \psi, \quad (3)$$

$$Z_n(Z, \Phi) = X_p(Z, \Phi)\sin \psi + Z_p(Z, \Phi)\cos \psi, \quad (4)$$

where  $\psi$  is the angle between the  $X(X_p)$ -axis and the  $X_n$ -axis,

$$X_p(Z, \Phi) = X(Z, \Phi), \quad (5)$$

$$Z_p(Z, \Phi) = Z\sin \epsilon - Y(Z, \Phi)\cos \epsilon. \quad (6)$$

We give the formulas for viewing angle  $\theta$ , Doppler factor  $\delta$ , apparent transverse velocity  $v_{\text{app}}$  and elapsed time  $T$  after ejection as follows.

- Viewing angle  $\theta$

$$\theta = \arccos[\cos \Delta(\cos \epsilon + \sin \epsilon \tan \Delta_p)]. \quad (7)$$

Where

$$\Delta = \arctan \left[ \left( \frac{dX}{dZ} \right)^2 + \left( \frac{dY}{dZ} \right)^2 \right]^{1/2}, \quad (8)$$

$\Delta$  is the angle between the spatial velocity vector and the  $Z$ -axis, and

$$\Delta_p = \arctan \left( \frac{dY}{dZ} \right) \quad (9)$$

is the projection of  $\Delta$  on the  $(Y, Z)$ -plane.

- Apparent transverse velocity  $v_{\text{app}}$  and Doppler factor  $\delta$

$$v_{\text{app}} = c\beta_{\text{app}} = \frac{c\beta\sin \theta}{1 - \beta\cos \theta}, \quad (10)$$

and

$$\delta = \frac{1}{\Gamma(1 - \beta\cos \theta)}, \quad (11)$$

where  $\beta = \frac{v}{c}$ ,  $v$  is the spatial velocity of the knot, and  $\Gamma = (1 - \beta^2)^{-1/2}$  is the Lorentz factor.

- Elapsed time  $T$ , at which the knot reaches the axial distance  $Z$ :

$$T = \int_0^Z \frac{1+z}{\Gamma\delta v\cos \Delta_s} dZ, \quad (12)$$

where  $z$  is the redshift of B1308+326,

$$\Delta_s = \arccos \left[ \left( \frac{dX}{dZ} \right)^2 + \left( \frac{dY}{dZ} \right)^2 + 1 \right]^{-1/2}, \quad (13)$$

where  $\Delta_s$  is the instantaneous angle between the velocity vector and the  $Z$ -axis.

All coordinates and amplitude  $A(Z)$  are measured in units of milliarcsecond (mas).  $\theta$  and  $\nu$  are instantaneous quantities at an elapsed time  $T$ .

### 3. Collimated trajectory and precessing jet model

In order to model-fit the source kinematics, an appropriate formalism is needed to describe the motion of superluminal components. We assume that each of the VLBI components moves along a curved (collimated) trajectory with a constant phase ( $\Phi = \text{const.}$ ) but that for successive knots, the phase changes due to precession. In this paper, we choose the following form for describing the collimated trajectory of the knots.

The amplitude  $A(Z)$  of the collimated trajectory as a function of  $Z$  is taken as:

$$A(Z) = A_0 \frac{2b}{\pi} \sin\left(\frac{\pi Z}{2b}\right), \quad (14)$$

when  $Z \leq b$ , and

$$A(Z) = A_0 \frac{2b}{\pi}, \quad (15)$$

when  $Z > b$ .

Parameter  $b$  may be regarded as a ‘‘collimation parameter’’ to describe the form of jet collimation. The phase  $\Phi$  is defined by parameter  $\phi$  for a specific trajectory:

$$\Phi = \phi + \Phi_0, \quad (16)$$

where  $\Phi_0$  is an arbitrary constant taken as 3.783 rad and  $\phi$  is defined as the precessing phase. Since  $\frac{d\Phi}{dZ} = 0$ , we have

$$\frac{dX}{dZ} = \frac{dA}{dZ} \cos \Phi, \quad (17)$$

$$\frac{dY}{dZ} = \frac{dA}{dZ} \sin \Phi. \quad (18)$$

Thus, from Eqs. (8), (9) and (13) we have

$$\Delta = \arctan\left(\frac{dA}{dZ}\right), \quad (19)$$

$$\Delta_p = \arctan\left(\frac{dA}{dZ} \sin \Phi\right), \quad (20)$$

$$\Delta_s = \arccos\left[\left(1 + \left(\frac{dA}{dZ}\right)^2\right)^{-1/2}\right]. \quad (21)$$

Substituting  $\Delta$ ,  $\Delta_p$ , and  $\Delta_s$  into Eqs. (7) and (10)–(12), we can calculate the viewing angle  $\theta$ , apparent velocity  $\beta_{\text{app}}$ , Doppler factor  $\delta$  and elapsed time  $T$ .

We should point out that the assumed form for describing the common precessing trajectory of the superluminal components shown in Fig. 2 is mathematically very simple, but it still closely represents the real jet field structure configurations observed in blazars. For example, the giant radio galaxy M 87, which has a powerful optical-radio jet and a supermassive black hole of  $\sim 6 \times 10^9 M_\odot$ , is the best possible target for studying the initial jet formation/collimation process (Biretta et al. 2002). Nakamura & Asada (2013) (also, Asada & Nakamura 2012; Doeleman et al. 2012) have found that its innermost jet emission components follow an extrapolated parabolic streamline with a nearly five orders of magnitude in the distance starting from the vicinity of the supermassive black hole, less than ten Schwarzschild radii.

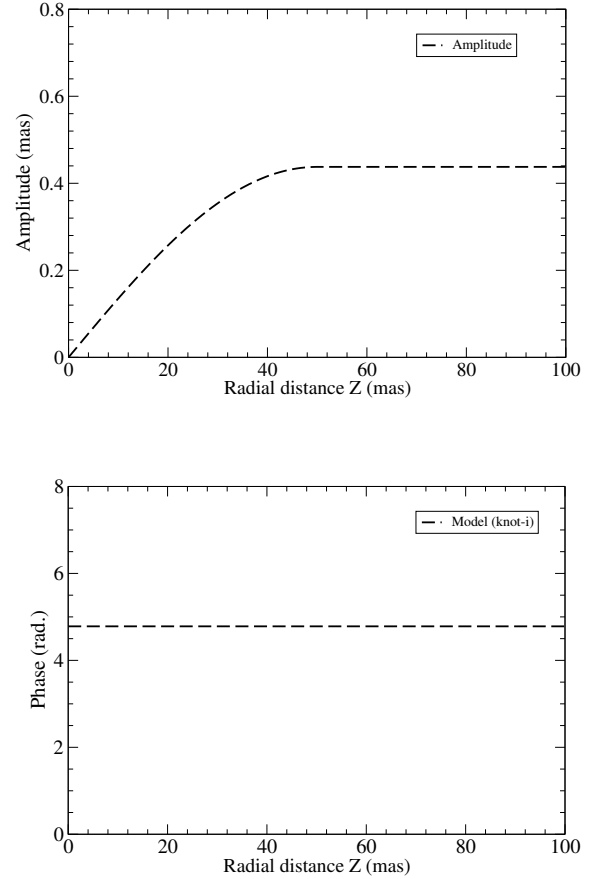


**Fig. 2.** The assumed amplitude function  $A(Z)$  and phase  $\Phi$  for describing the trajectory of a knot. Here  $\Phi = 4.783$  rad, corresponding to a precession phase  $\phi = 1.0$  rad,  $\Phi_0 = 3.783$  rad. We refer to the text for further details.

They have also proposed a magnetohydrodynamic (MHD) nozzle model to interpret the property of the bulk jet acceleration and have assumed that the MHD nozzle consists of a hollow parabolic tube.

Moreover, general relativistic MHD simulations (e.g., McKinney et al. 2012) reveal that the magnetic field structures (configurations) near the horizon of a rotating black hole closely correspond to a parabolic configuration, which is consistent with the analytic results given by Beskin & Zheltoukhov (2013) for a field geometry consisting of a radial field near the horizon and a vertical field far from the black hole. In these configurations, the distribution of the magnetic field and the field angular velocity profile near the horizon can be described in more detail (Punsly 2001; McKinney et al. 2012; Beskin & Zheltoukhov 2013). In addition, Tateyama (2013) found that in the prominent blazar OJ287, the superluminal components were ejected along a fork-like structure.

Thus, the assumed shape for describing the common precessing trajectory (like that shown in Fig. 2), which has been previously applied to model-fit the kinematics in blazars 3C 279 (Qian 2011, 2012) and 3C 454.3 (Qian et al. 2014), is quite similar to those discussed in Nakamura & Asada (2013; also Asada & Nakamura 2012; Doeleman et al. 2012; McKinney et al. 2012; Beskin & Zheltoukhov 2013). In addition, the assumed pattern is also quite similar to the fork structure observed in the prominent blazar OJ287 by Tateyama (2013). We refer to the distributions of the modeled precessing trajectories shown in Figs. 3 and 4

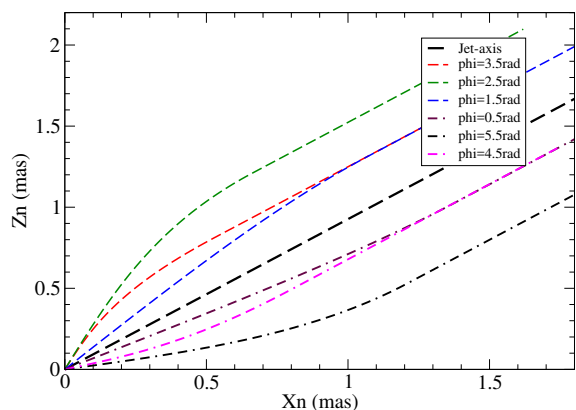


**Fig. 3.** Modeled distribution of the trajectories produced by the precessing jet-nozzle model for precession phases  $\phi = 3.5, 2.5, 1.5, 0.5, 5.5$  and  $4.5$  radians. The jet-axis is at  $PA = -47.2^\circ$ . The common trajectory rotates around the jet axis clockwise viewed along the axis.

below. Our model is consistent with the axisymmetric case of MHD theories for formation of relativistic jets.

In this paper we adopt the concordant cosmology model with  $\Omega_\Lambda = 0.73$ ,  $\Omega_m = 0.27$  and Hubble constant  $H_0 = 71 \text{ km s}^{-1} \text{ Mpc}^{-1}$  (Spergel et al. 2003). For the redshift  $z = 0.997$  of B1308+326, we have its luminosity distance  $D_L = 6.61 \text{ Gpc}$  and the angular diameter distance  $D_A = 1.66 \text{ Gpc}$  (Hogg 1999; Pen 1999). The angular scale is  $1 \text{ mas} = 8.04 \text{ pc}$  and the proper motion of  $1 \text{ mas/yr}$  is equivalent to an apparent velocity of  $52.34c$ .

## 4. Model fitting the kinematics

### 4.1. Introduction

B1308+326 is a high-redshift quasar ( $z = 0.997$ ) and has been detected by the *Fermi* Gamma-ray Observatory (Ackermann et al. 2011, 2013, Acero et al. 2015). In historical records it was observed as being optically variable with a long-term variability amplitude of  $\sim 5.6 \text{ mag}$  in  $B$ -magnitude (Angel & Stockman 1980) and as having highly variable optical polarization, and was classified as one of the most variable BL Lac objects. Recently, flares in NIR bands were observed during the *Fermi* LAT source monitoring program in June 2012 (Carrasco et al. 2012) and it become one of the prominent blazars (Puschell et al. 1979; Sitko et al. 1984, 1985; Piner et al. 2012). B1308+326 radiates across the entire electromagnetic spectrum from radio-optical-X-ray to  $\gamma$ -ray. Very strong variability has been observed in all these wavebands with various timescales (hours/days to years). Cassaro et al. (2002) found that the orientation of the jet on pc-scales is misaligned with that on kpc-scales, following a curved path.

Recently, its mas-scale structure and kinematics have been investigated by Britzen et al. (BQS17), who performed a re-analysis of the 15 GHz observations performed with the VLBA within the MOJAVE programme<sup>2</sup>. They found that the ejection position angle of the superluminal components changed in a rather wide range of  $\sim 50^\circ$ . Based on the 15 GHz VLBI observations by Britzen et al. for the period 1995–2013, we can briefly summarize its properties as follows.

- It can be seen from the VLBI maps that the structure of the source experienced an evolutionary process: from single

<sup>2</sup> The MOJAVE database is maintained by the MOJAVE team (Lister et al. 2009).

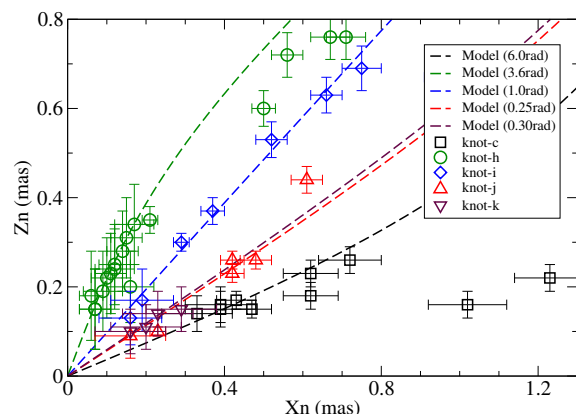


**Fig. 4.** Modeled distribution of the trajectories of knots *c*, *h*, *i*, *j* and *k*. Within a core separation of  $\sim 0.5 \text{ mas}$ , all the inner trajectories can be well fitted by the precessing nozzle model.

core (1995)  $\implies$  fully developed core-jet structure (2000–2008)  $\implies$  recovered to a contracted core-jet structure with a single dominated core plus a weak diffuse component (2009–2010)  $\implies$  starting a new core-jet structure (2014), seemingly having a quasi-periodicity of  $\sim 15 \text{ yr}$ .

- During the period of fully developed core-jet structure, the entire jet has a curved helical pattern, formed by the sequentially ejected superluminal knots with isolated individual trajectories. This might indicate that the superluminal components were ejected by jet-nozzle precession. In fact, the jet position angle swing is quite clear: Knot *c* and knot *h* have position angles  $\sim -70^\circ$  and  $\sim -20^\circ$ , respectively. Their trajectories roughly form the (projected) jet cone (or the outer boundaries of the distribution of the knots' trajectories), revealing the jet position angle swing of  $\sim 50^\circ$ .
- The trajectories of knots *c*, *h*, *i*, *j* and *k* have rather regular shapes within core separations  $\sim 0.3\text{--}0.5 \text{ mas}$  (almost ballistic tracks ejected from the core). Thus we can convincingly determine their ejection position angles and study the jet swing mechanism.
- The ejection times of knots *c* and *h* have been derived from the VLBI observations to be  $\sim 1995.73$  and  $\sim 2002.30$ . The time difference is  $6.57 \text{ yr}$  (BQS17). If the position angle swing is due to precession, then the precession period should be  $> 13 \text{ yr}$ .

### 4.2. Selection of model parameters

The jet swings observed in blazars have been interpreted in terms of different mechanisms (Agudo 2009). These include instabilities in accretion disk or interaction between jet and its environment (e.g., Hardee 1987; Dhawan et al. 1998); helical motion of the superluminal components (or shocks) (e.g., Qian et al. 1991; Steffen et al. 1995; Vicente et al. 1996; Valtonen & Pihajok 2013; Molina et al. 2014; Qian 2016); and jet precession caused by the orbital motion of a black hole binary (e.g., Britzen et al. 2001; Kun et al. 2015). Regular swings are usually explained in terms of the precession of an entire jet or the precession of a jet-nozzle (e.g., Stirling et al. 2003; Tateyama & Kingham 2004; Lister et al. 2009; Qian 2012, 2013; Qian et al. 2014).

The precessing jet nozzle model is different from the precessing jet model. In the precessing jet model, the whole jet rotates as it precesses and the ejected knots move along the jet axis. However, in the precessing jet nozzle model, the jet nozzle precesses

**Table 1.** Parameters selected for the precessing nozzle model.

$\epsilon$	$1.5^\circ$
$\psi$	$-42.8^\circ$
$\theta_{\text{jet}}$	$1.5^\circ$
$A_0$	$1.375 \times 10^{-3}$
$b$	50 mas
$\eta$	$0.79^\circ$
$\Phi_0$	3.783 rad
$T_p$	$16.9 \pm 0.3$ yr

around a fixed jet axis and the knots are ejected from the nozzle, moving along their own individual trajectories (plane or helical, Qian 2016) with different bulk Lorentz factors. The precession of the nozzle leads to the rotation of the ejection direction of the knots or the ejection position angle swing. The combination of a sequence of isolated knots ejected from this nozzle would exhibit the structure of the whole jet and the evolution of the structure seen on VLBI-maps (e.g., Tateyama & Kingham 2004; Qian et al. 2009, 2014; Tateyama 2009, 2013).

In order to model fit the kinematics of the superluminal knots in terms of our precessing jet-nozzle model, we need to select two sets of model parameters:

- Geometric and kinematic parameters which include: parameters  $\epsilon$  and  $\psi$  defining the orientation of the jet axis; amplitude function  $A(Z)$  and  $b$  for describing the shape of the precessing common trajectory; and the Lorentz factor ( $\Gamma$ ) for each of the knots. Based on the observed kinematic features of the knots we can deduce a preliminary set of these parameters. For example, if the viewing angle of the jet is given, then (i) the shape of the precessing common trajectory (the function  $A(Z)$  and parameter  $b$ ) can be roughly determined from the observed shapes of the knots' trajectories; (ii) from the observed (approximate) symmetric distribution of the trajectories of the knots, the position angle of the jet-axis and its spatial orientation ( $\psi$ ) can be estimated (see Figs. 3–4 below); and (iii) the Lorentz factors of the knots can be estimated from their observed apparent velocities. The selection of these parameters are not unique, largely depending on the viewing angle of the jet (or parameter  $\epsilon$ ). They are selected through trial model fittings of the kinematics of the knots, using the formalism described in Sects. 2 and 3. Since different viewing angles selected for the jet axis would cause different projection effects and thus lead to different geometric and kinematic parameters, we should choose an appropriate value for parameter  $\epsilon$ . In this paper we take  $\epsilon = 1.5^\circ$ . The reason is that the maximal apparent velocity observed in the source is  $\sim 23c$  (for knot *c*, see Sect. 4.3.1.) and the critical viewing angle is  $\sim 2.5^\circ$ . We take a smaller viewing angle which is similar to the jet inclination ( $1.65^\circ \pm 0.45^\circ$ ) estimated by BQS17.
- Parameters that describe the kinematic behaviors of the knots changing with time: the ejection times  $t_0$  of the knots and the precession period  $T_p$ . Although the geometric and kinematic parameters are not uniquely selected, the model ejection times ( $t_0$ ) and the precession period  $T_p$  are strictly constrained by the observed ejection times ( $t_{0,\text{obs}}$ , see Table 3) and the observed distribution of the trajectories (see Fig. 4). We can select this set of model parameters as follows. The observed ejection times ( $t_{0,\text{obs}}$ ) derived from the VLBI measurements can be used as the approximate values for the model ejection times ( $t_0$ ). Usually,  $t_{0,\text{obs}}$  of a knot is derived from extrapolating its core separation to zero by

**Table 2.** Precessing nozzle model parameters ( $T_p = 16.9$  yr).

$\phi$ (rad)	$t_0$	PA(deg)	$\theta$ (deg)
6.2832( $2\pi$ )	1994.78	-64.96	2.07
6.0	1995.54	-69.76	1.92
5.5	1996.89	-76.52	1.59
5.0	1998.24	-78.74	1.21
4.5	1999.58	-69.90	0.85
4.0	2000.93	-42.72	0.72
3.5	2002.27	-20.24	0.94
3.0	2003.62	-15.56	1.32
2.5	2004.96	-19.48	1.69
2.0	2006.31	-26.98	2.00
1.5	2007.66	-36.06	2.20
1.0	2009.00	-45.80	2.29
0.5	2010.35	-55.62	2.24
0.0	2011.69	-64.96	2.07

**Notes.** The table lists: precession phase  $\phi$ , ejection epoch  $t_0$ , initial position angle PA and initial viewing angle  $\theta$ .

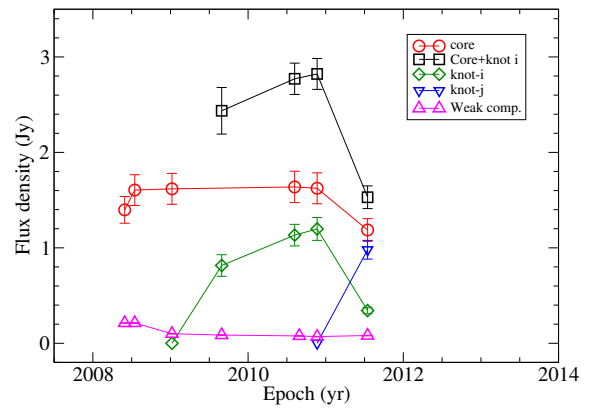


**Fig. 5.** The variations of the flux density of the core (red circles), core plus knot *i* (black squares), weak components (magenta up-triangles), knot *i* (green diamonds) and knot *j* (maroon down-triangles) (see parts VI–V of Table 2 in BQS17). During the period 2008.54–2010.89 the core flux density is stable at  $\sim 1.6$  Jy and the light curve of knot *i* can be derived, assuming the core flux to be 1.62 Jy at 2009.66. This clearly indicates that knot *i* was ejected before 2009.66. Taking the rising time of the outburst produced by knot *i* to be  $\sim 0.7 \pm 0.3$  yr, we can infer that knot *i* was ejected at  $\sim 2009.0 \pm 0.3$  yr.

linear regression (BQS17). If trajectories are non-radial, this method could induce significant errors in  $t_{0,\text{obs}}$ . In addition, it can be seen from Fig. 4 that the trajectories of knots *c* and *h* approximately define the aperture of the jet cone (projected) and the time difference between their ejection epochs (1995.73 and 2002.30; BQS17) is 6.57 yr. Thus we can infer that the precession period should be  $> 13$  yr, because the aperture of the real jet cone may be larger than that defined by the trajectories of knots *c* and *h*. So we can search for an appropriate precession period through the model fitting of the source kinematics within a period range of  $\sim 14$ –20 yr.

We perform the model fitting of the kinematics of five knots *c*, *h*, *i*, *j*, *k* to search for the precession period, because these knots have rather regular structures and consistent kinematic properties on scales of core separation  $r_n \lesssim 0.5$  mas.

Since for each knot, five kinematic relations ( $Z_n - X_n$ ,  $r_n(t)$ ,  $X_n(t)$ ,  $Z_n(t)$ , and  $\beta_{\text{app}}(t)$ ) need to be modeled (a total of twenty-five relations for five knots *c*, *h*, *i*, *j* and *k*), this is a procedure of model-fitting multiple functional relations using multiple

**Table 3.** Parameters for the superluminal knots *c*, *h*, *i*, *j* and *k*.

Knot	$t_0$	PA (deg)	$\phi$ (rad)	$\theta$ (deg)	$\Gamma$	$t_{0,\text{obs}}$
<i>c</i>	1995.54	-69.76	6.0	1.92	26	1995.73
<i>h</i>	2002.00	-23.06	3.6	0.87	15	2002.30
<i>i</i>	2009.00	-45.80	1.0	2.29	10	2010.01
<i>j</i>	2011.02	-60.39	0.25	2.17	15.5	2010.81
<i>k</i>	2010.88	-59.45	0.30	2.19	9.1	2010.64

**Notes.** Their kinematics within core separation  $r_n \lesssim 0.5$  mas are consistently explained in terms of the precessing jet-nozzle model: modeled ejection epoch  $t_0$ , ejection position angle PA(deg), precession phase  $\phi$ (rad), initial viewing angle  $\theta$ (deg), initial Lorentz factor  $\Gamma$  and the observed ejection times  $t_{0,\text{obs}}$  (taken from BQS17).

parameters. Moreover, the observed initial position angles and ejection times of the five knots do not constitute a statistical sample, and standard statistical methods (e.g., Fourier transform and discrete autocorrelation methods) cannot be applied for an analysis of periodicity. Thus we find the precession period through an analytical modeling of the kinematics of the knots with an estimation of its uncertainty (see Figs. 6–8 below). Therefore, the model fitting results obtained in this paper are tentative interpretations of the kinematics of the features in the jet of the quasar B1308+326. The set of model parameters selected through trial model fittings and relevant modeled data are shown in Tables 1–3. In Figs. 3–4, the modeled distribution of the trajectories is shown, as well as the fits to the trajectories of knots *c*, *h*, *i*, *j* and *k*. The precession period is determined as  $T_p = 16.9$  yr and the modeled ejection epochs of the knots  $t_0$  are calculated from the following equation (also see Tables 2 and 3).

$$t_0 = 1995.54 + \frac{T_p}{2\pi}(6.0 - \phi). \quad (22)$$

We should point out that for knots *c*, *h*, *j* and *k*, the modeled ejection epochs ( $t_0$ ) are different from the observed ones ( $t_{0,\text{obs}}$ ) derived from the VLBI observations (BQS17; see Table 3) by  $-0.19$  yr,  $-0.30$  yr,  $+0.21$  yr and  $+0.24$  yr, respectively. These values indicate that the modeled ejection times are consistent with the observed ones within the errors of the measurements and are well determined. However, for knot *i*, the observed position angle is  $\sim -46^\circ$ , corresponding to a precession phase  $\phi = 1.0$  rad. Thus its modeled ejection epoch  $t_0$  derived from Eq. (22) is 2009.0, which is different from the observed one  $t_{0,\text{obs}} = 2010.01$  by  $-1.01$  yr. That is, we chose an earlier date for its ejection. Fortunately, this choice is supported by the observational fact (see Fig. 5): the observed flux density of the core rapidly increased by  $\sim 0.82$  Jy at 2009.66, which clearly indicates that knot *i* had been ejected before 2009.66. Assuming that the rising time of the radio outburst produced by the emergence of knot *i* is  $\sim 0.7 \pm 0.3$  yr (at 15 GHz), we can reasonably obtain its ejection epoch to be  $2009.0 \pm 0.3$  yr. Some studies of the flux density evolution of superluminal components have revealed that the rising times of radio outbursts caused by the emergence of superluminal components are usually in the range of  $\sim 0.3$ – $1.5$  yr at 15 GHz (e.g., Qian et al. 1996, 2010; Qian 1996a, b). Thus, the choice of the ejection epoch for knot *i* is consistent with some theoretical modeling results. For example, the study of the apparent and intrinsic flux evolution of knot C4 in blazar 3C 345 shows (Qian et al. 1996) that its rising time of  $\sim 0.5$  yr (at 22 GHz) was due to the field magnification and acceleration of relativistic electrons in the knot. Here for knot *i*, its kinematic features have been determined and the intrinsic flux evolution can be studied in detail, but this is beyond the scope of this paper. Obviously,

the observed flux density evolution of knot *i* and the above arguments are important for the applicability of our precessing nozzle model.

The ingredients causing the discrepancies between the modeled jet ejections and the ones derived from the VLBI observations by BQS17 are not clear. In general, this could be mainly due to the working hypotheses made in the VLBI measurements: Superluminal components move along straight lines with uniform speeds. However, there are other ingredients which could affect the determination of ejection times. These may include insufficient data sampling within core separations less than  $\sim 0.1$ – $0.3$  mas; initial acceleration; trajectory curvature (non-ballistic motion); and radio flux density evolution and opacity effects. The effects of these ingredients could be different for different components. Obviously in the case of knot *i*, its initial motion with a lower Lorentz factor (and Doppler boosting) and the rise of its flux density may be the main causes for the discrepancy (see Fig. 8).

Lister et al. (2013) found that the inner jet position angle of B1308+326 swings in the range of  $-30^\circ$  to  $-80^\circ$ , which is consistent with our data, but they found that its jet-swing has a quasi-period of  $\sim 5.1$  yr, which is different from the assumed precession period of  $16.9 \pm 0.3$  yr here. This might be mainly due to the different definitions of “jet position angle”. In Lister et al., the inner jet position angle is defined as the flux-density weighted average position angle of the components in the core separation range from 0.15 mas to 1.0 mas, while what we defined is the position angle of the knots ejected by the precessing jet-nozzle.

#### 4.3. Model-fitting results for knots *c*, *h*, *i*, *j*, *k*, and *d*

Using the model parameters selected above (Table 1), we can discuss the results of the model fitting for the superluminal components observed in the quasar B1308+326 (with VLBI-data given in BQS17). The kinematics of the ten knots *c*, *d*, *h*, *i*, *j*, *k*, *f*, *a*, *e* and *g* are model-fitted. We will first describe the results of model-fitting the kinematics of six knots (*c*, *h*, *i*, *j*, *k*, *d*), which are given in Figs. 6–8 and A.1–A.3.

##### 4.3.1. Knot *c*

As shown in Fig. 4, knot *c* has a curved trajectory and the model fitting of its kinematics has to be split into two parts: The inner trajectory (within a core separation of  $\sim 0.8$  mas) and the outer trajectory (with core separations beyond  $\sim 0.8$  mas).

- Its inner trajectory has a regular pattern and can be model fitted in terms of the precessing nozzle model. Its ejection epoch  $t_0 = 1995.54$  (corresponding to a precessing phase

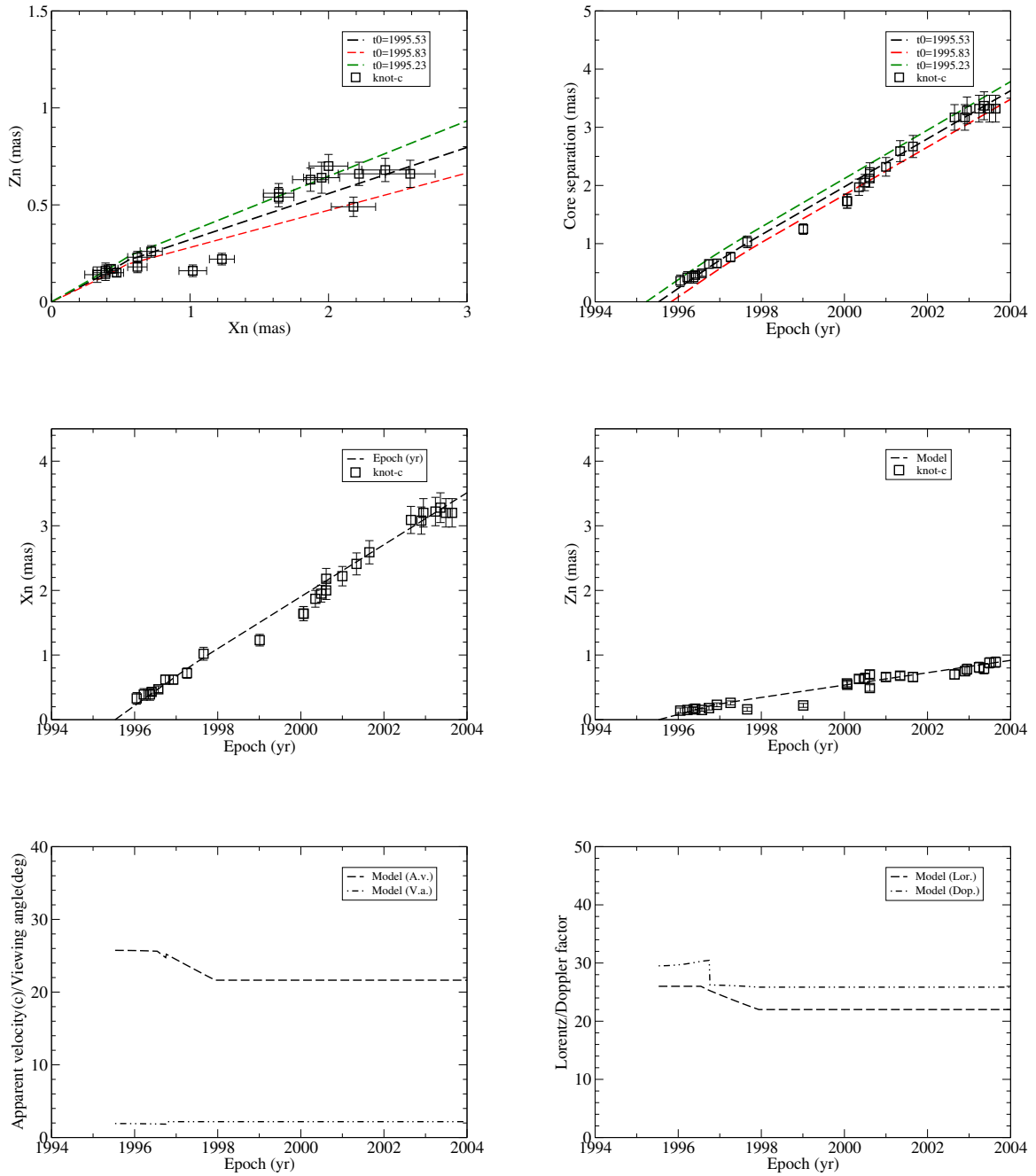


**Fig. 6.** Model fitting of the kinematics for knot *c*: trajectory  $X_n$ - $Z_n$ , core separation  $r_n(t)$ , coordinates  $X_n(t)$  and  $Z_n(t)$ , the modeled apparent velocity/viewing angle and Lorentz/Doppler factor. The inner trajectory with the core separation less than  $\sim 0.8$  mas is fitted by the precessing jet-nozzle model and the outer trajectory is fitted by introducing changes of the amplitude function  $A(Z)$ . In the *upper plots*, two additional (red and green) curves calculated for ejection times  $= t_0 + 0.3$  yr and  $t_0 - 0.3$  yr are shown, indicating that most of the observational data points are within the regions confined by the two curves and the precession period is determined with an uncertainty of  $\sim 0.3$  yr.

$\phi = 6.0$  rad). The model-fitting results are shown in Fig. 6, including the trajectory  $(X_n, Z_n)$ , core separation  $r_n(t)$ , coordinates  $X_n(t)$  and  $Z_n(t)$ , and the modeled apparent velocity/viewing angle and bulk Lorentz factor/Doppler factor. The fitting of its inner trajectory is consistent with those of the other five knots (*d*, *h*, *i*, *j*, *k*), indicating that the precessing nozzle model is applicable to the inner trajectories of these knots.

- Its outer trajectory (with core separations beyond  $\sim 0.8$  mas) deviates from the precessing common trajectory. This deviation could be caused by other ingredients (e.g.,

Kelvin-Helmholtz instabilities due to interaction between the knot and the surrounding medium; Hardee 1987), which need to be additionally considered in the fitting.

To explain this trajectory curvature, we have to introduce changes of the amplitude function  $A(Z)$  relative to its inner trajectory. For simplicity, four additional parameters ( $z_1, z_2, w_1, w_2$ ) are introduced to describe the amplitude function  $A(Z)$  in the outer trajectory region, assuming that knot *c* moves outward and is retained in its ejection plane defined by the precessing nozzle

model<sup>3</sup>. The amplitude function for describing the entire trajectory is then given as follows.

For  $Z \leq z_1$  (inner trajectory region),  $A(Z)$  is described by Eq. (14), following the precessing common trajectory:

$$A(Z) = A_0 \left( \frac{2b}{\pi} \right) \sin \left( \frac{\pi Z}{2b} \right). \quad (23)$$

For  $z_1 < Z < z_2$ ,

$$A(Z) = A_1 + w_1(Z - z_1). \quad (24)$$

For  $Z > z_2$ ,

$$A(Z) = A_1 + w_1(z_2 - z_1) + w_2(Z - z_2). \quad (25)$$

Here  $A_1 = A_0 \left( \frac{2b}{\pi} \right) \sin \left( \frac{\pi z_1}{2b} \right)$ .  $Z > z_1$  represents the outer trajectory region. When  $z_2 \neq z_1$  and  $w_2 \neq w_1$ , Eqs. (24) and (25) describe the trajectory having two curvatures.

For knot *c*, we assume  $z_1 = z_2 = 18$  mas,  $w_1 = w_2 = 0.020$ . For the fitting of its core separation versus time it is required that knot *c* decelerates along the trajectory: For  $Z \leq 15$  mas,  $\Gamma = 26$ ; for  $15 \text{ mas} < Z < 32$  mas,  $\Gamma = 26 - 4(Z - 15)/17$ ; and for  $Z > 32$  mas  $\Gamma = 22$ .

It can be seen from Fig. 6 that the trajectory  $Z_n$ - $X_n$ , core separation  $r_n(t)$ , coordinates  $X_n(t)$  and  $Z_n(t)$  are fitted well. The modeled apparent velocity ( $22$ – $26c$ ) is consistent with the averaged value  $22.9 \pm 0.5c$  ( $0.437 \pm 0.010$  mas/yr) given in BQS17. In addition, Fig. 6 shows two additional model curves (red and green) calculated for ejection times  $t_0 + 0.30$  yr and  $t_0 - 0.3$  yr, indicating that most of the observational data points are within the regions confined by the two curves and the precession period is determined with an uncertainty of  $\sim 0.3$  yr.

#### 4.3.2. Knot *h*

As seen from Fig. 5, knot *h* has a curved trajectory structure and thus its model fitting has to be split into two parts (as like for knot *c*): the inner trajectory (with the core separation less than  $\sim 0.5$  mas) and the outer trajectory (with the core separation beyond  $\sim 0.5$  mas).

- The inner trajectory of knot *h* is quite regular and closely follows the precessing common trajectory pattern. Its kinematics in this region can be well fitted by the precessing nozzle model. Its ejection epoch  $t_0 = 2002.0$  ( $\phi = 3.6$  rad). The fitting results are shown in Fig. 7, including the trajectory ( $X_n, Z_n$ ), core separation  $r_n(t)$ , coordinates  $X_n(t)$  and  $Z_n(t)$ , the modeled apparent velocity/viewing angle and bulk Lorentz/Doppler factor. In addition, Fig. 7 shows two additional model curves (red and green) calculated for ejection times  $t_0 + 0.3$  yr and  $t_0 - 0.3$  yr, demonstrating that most of the observational data points are within the regions confined by the two curves and that the precession period is determined with an uncertainty of  $\sim 0.3$  yr.
- Its outer trajectory apparently deviates from the precessing common trajectory pattern (see Fig. 4). In order to fit its outer trajectory, we have to introduce changes of the amplitude function  $A(z)$  as for knot *c*. In this case we assume that the trajectory amplitude function  $A(Z)$  is described by Eqs. (23)–(25) with  $z_1 = z_2 = 23$  mas and  $w_1 = w_2 = -0.005$ .

For the fitting of the core separation versus time, a slight bulk acceleration is required: For  $Z \leq 23$  mas  $\Gamma = 15$ ; for  $23 \text{ mas} < Z < 44$  mas  $\Gamma = 15 + (Z - 23)/21$ ; and for  $Z > 44$  mas  $\Gamma = 16$ .

It can be seen from Fig. 7 that all the kinematic features ( $Z_n$ - $X_n$ ,  $r_n(t)$ ,  $X_n(t)$  and  $Z_n(t)$ ) are fitted well. The modeled apparent velocity varies along the trajectory from  $\sim 6.5c$  to  $\sim 12.6c$ .

#### 4.3.3. Knot *i*

Knot *i* was observed within a core separation of  $\sim 1.2$  mas. It reveals a ballistical motion and the entire trajectory (both inner and outer regions) can be well fitted in terms of the precessing nozzle model, closely following the precessing common trajectory. Its ejection epoch is taken as  $t_0 = 2009.0$ , as argued before, corresponding to the precessing phase  $\phi = 1.0$  rad. In order to fit its core separation versus time, an initial bulk acceleration is required: For  $Z \leq 5$  mas  $\Gamma = 10$ ; for  $Z = 5$ – $10$  mas  $\Gamma = 10 + 7(Z - 5)/5$ ; and for  $Z > 10$   $\Gamma = 17$ .

The fitting results are shown in Fig. 8. It can be seen that its kinematics can be well fitted. In addition, Fig. 8 shows two additional model curves (red and green) calculated for ejection epochs  $t_0 + 0.3$  yr and  $t_0 - 0.3$  yr, demonstrating that most of the observational data points are within the regions confined by the two curves and that the precession period is determined with an uncertainty of  $\sim 0.3$  yr. The modeled apparent velocity (from  $\sim 6.8c$  to  $\sim 14c$ ) during the period of 2010.5–2012 is much smaller than the average value  $16.1 \pm 2.3c$  ( $0.308 \pm 0.043$  mas/yr) derived in BQS17. This is because its ejection epoch has been shifted to 2009.0 (one year earlier than that given in BQS17) and an initial bulk acceleration has to be introduced.

#### 4.3.4. Knot *j*

Knot *j* was observed within a core separation of  $\sim 0.75$  mas. Its entire trajectory can be explained in terms of the precessing nozzle model, closely following the precessing common trajectory. Its ejection epoch is  $t_0 = 2011.02$  (corresponding to a phase  $\phi = 0.25$  rad). The Lorentz factor is constant,  $\Gamma = 15.5$ .

The fitting results are shown in Fig. A.1. In addition, Fig. A.1 shows two additional model curves (red and green) calculated for ejection epochs  $t_0 + 0.3$  yr and  $t_0 - 0.3$  yr, demonstrating that most of the observational data points are within the regions confined by the two curves and that the precession period is determined with an uncertainty of  $\sim 0.3$  yr. The modeled apparent velocity,  $\sim 13.0c$ , is comparable to the average value  $11.7 \pm 1.2c$  ( $0.223 \pm 0.022$  mas/yr) derived in BQS17.

#### 4.3.5. Knot *k*

Knot *k* was observed within a core separation of  $r_n \sim 0.33$  mas. Its entire trajectory (the observed inner trajectory only) can be explained in terms of the precessing nozzle model, closely following the precessing common trajectory. The ejection epoch is  $t_0 = 2010.88$  (corresponding to a phase  $\phi = 0.30$  rad). The Lorentz factor is assumed to be constant,  $\Gamma = 9.1$ .

The fitting results are shown in Fig. A.2. In addition, Fig. A.2 shows two additional model curves (red and green) calculated for ejection times  $t_0 + 0.3$  yr and  $t_0 - 0.3$  yr, indicating that most of the observational data points are within the regions confined by the two curves and that the precession period is determined with an uncertainty of  $\sim 0.3$  yr. The modeled apparent velocity  $\sim 5.6c$  is very consistent with the average value  $5.1 \pm 0.4c$  ( $0.097 \pm 0.007$  mas/yr) derived in BQS17.

<sup>3</sup> It is also possible in the precessing jet nozzle model that the individual trajectories of the knots are helices with small pitch angles (i.e., a precessing helical model, see Qian 2016 for NRAO 150).

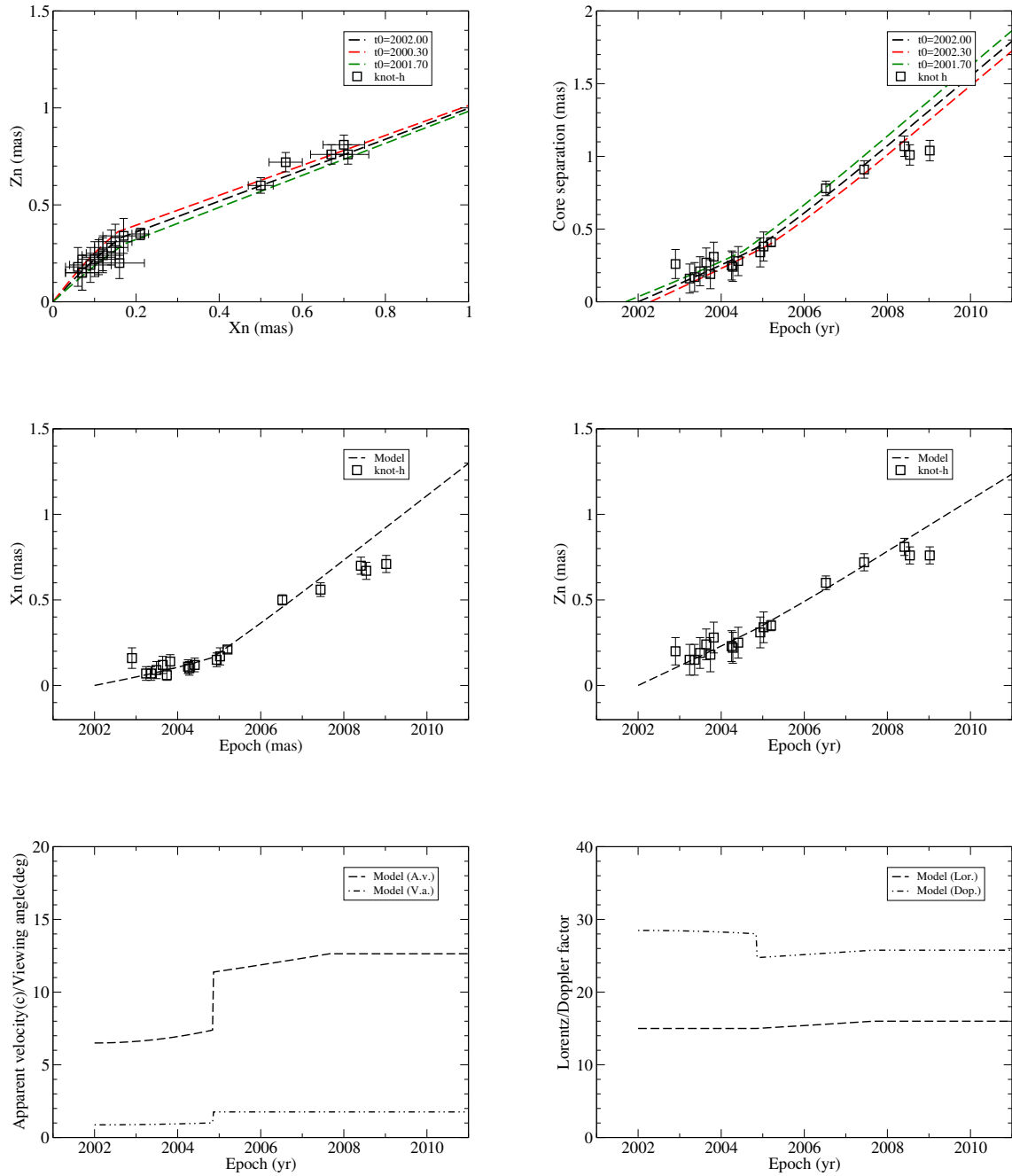


**Fig. 7.** Model fitting of the kinematics for knot *h*: trajectory  $Z_n$ - $X_n$ , core separation  $r_n(t)$ , coordinates  $X_n(t)$  and  $Z_n(t)$ , the modeled apparent velocity/viewing angle and Lorentz/Doppler factor. The inner trajectory is well fitted by the precessing jet nozzle model. The outer trajectory is fitted by introducing changes of its amplitude function  $A(Z)$ . An apparent acceleration from  $\sim 6.5c$  to  $\sim 12.6c$  is modeled. In the *upper plots*, two additional model (red and green) curves calculated for ejection times  $t_0 + 0.3$  yr and  $t_0 - 0.3$  yr are shown, indicating that most of the observational data points are within the regions confined by the two curves and that the precession period is determined with an uncertainty of  $\sim 0.3$  yr.

#### 4.3.6. Knot *d*

On the whole, the kinematics of knot *d* can be fitted by the precessing jet nozzle model within a core separation  $\sim 2.2$  mas. Its ejection epoch is assumed to be  $t_0 = 1994.23$  (corresponding to precessing phase  $\phi = 0.20$  rad). It is required that some initial bulk acceleration should be taken into account: For  $Z \leq 14.5$  mas,  $\Gamma = 12.0$ ; for  $14.5 \text{ mas} < Z < 20$  mas,  $\Gamma = 12 + 7(Z - 14.5)/5.5$ ; and for  $Z > 20$  mas,  $\Gamma = 19$ .

The fitting results of its kinematics are shown in Fig. A.3. The modeled apparent velocity varies along the trajectory in the range  $\sim 9$ – $17c$ .

#### 4.4. Model-fitting results for knots *f*, *a*, *e*, *g*

As pointed out by Qian (2012, 2013) and Qian et al. (2014), the trajectories of superluminal components observed in blazars have a variety of shapes, and curvature in trajectories often occurs at different core separations, revealing non-ballistic motions. This could make the recognition of jet-nozzle precession very difficult, especially if the inner trajectories of the knots are irregular or not observed. In blazars, only part of the knots can be fitted in terms of precessing nozzle model (Qian 2012, 2013). This is because multiple ingredients may affect the shapes of their trajectory, for example, in addition to their regular helical

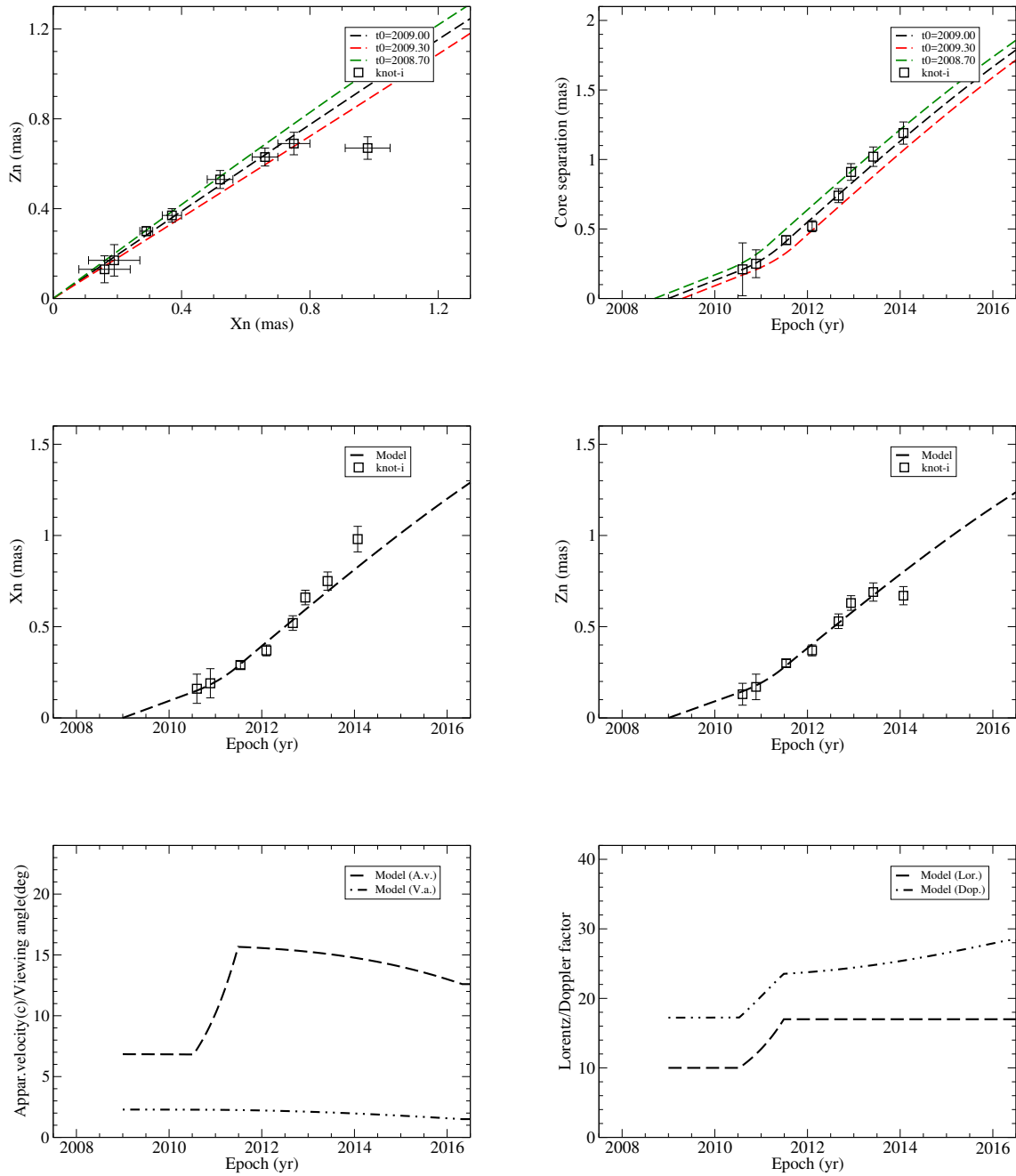


**Fig. 8.** Model fitting of the kinematics for knot  $i$ : trajectory  $Z_n$ - $X_n$ , core separation  $r_n(t)$ , coordinates  $X_n(t)$  and  $Z_n(t)$ , the modeled apparent velocity/viewing angle and Lorentz/Doppler factor. The initial acceleration is apparent (from  $\sim 6.8c$  to  $\sim 14c$ ). In the *upper plots*, two additional model (red and green) curves calculated for ejection epochs  $t_0 + 0.3$  yr and  $t_0 - 0.3$  yr are shown, indicating that most of the observational data points are within the regions confined by the two curves and that the precession period is determined with an uncertainty of  $\sim 0.3$  yr.

or ballistical motion, their trajectory could be changed by surrounding winds or through Kelvin-Helmholtz instabilities due to interaction between the superluminal components and the galactic/extragalactic media (e.g., Hardee 1987). This is the case for knots ( $f$ ,  $a$ ,  $e$ ,  $g$ ). Their trajectories were observed to be quite irregular with insufficient data sampling in the regions of core separation smaller than  $\sim 0.3$  mas. In order to model-fit their kinematics within the framework of our precessing nozzle model, we assume that their innermost trajectories (within core separations of  $\sim 0.1$ – $0.3$  mas) might still follow the precessing common trajectory, but that their outer trajectories (core separations beyond  $\sim 0.1$ – $0.3$  mas) have already deviated from the

precessing common trajectory. Therefore, we use the model-fitting approach similar to that for fitting the outer trajectories of knots  $c$  and  $h$ .

#### 4.4.1. Knot $f$

We may take knot  $f$  as an example.

The first two data-points at core separations of  $\sim 0.32$  mas and  $\sim 0.36$  mas indicate its position angles to be  $-66^\circ$  and  $-59^\circ$ , which are close to the position angle ( $-70^\circ$ ) predicted by the precessing nozzle model for its ejection time  $t_0 = 1995.66$

(corresponding to phase  $\phi = 5.95$  rad; BQS17). This seems to indicate that a slight curvature of its trajectory could have occurred at core separation smaller than  $\sim 0.3$  mas. Thus we assume its ejection time to be  $t_0 = 1995.66$  (BQS17) and its inner trajectory (with core separations less than  $\sim 0.3$  mas) can be fitted in terms of the precessing nozzle model. For explaining its outer trajectory (with core separations larger than  $\sim 0.3$  mas), we have to introduce two curvatures of its trajectory described by the changes of the amplitude function  $A(Z)$ :  $z_1 = 9$  mas,  $z_2 = 40$  mas,  $w_1 = -0.01$  and  $w_2 = 0.030$ .

For fitting the kinematics of knot **f**, bulk acceleration is required: For  $Z \leq 9$  mas,  $\Gamma = 13.5$ ; for  $Z = 9-75$  mas  $\Gamma = 13.5 + 3(Z-9)/66$ ; and for  $Z > 75$  mas  $\Gamma = 16.5$ .

The results of the fitting process are shown in Fig. A.4.

#### 4.4.2. Knot **a**

Knot **a** has only two data points within a core separation of  $\sim 0.5$  mas. Such insufficient data sampling makes the model fitting quite uncertain. We assume that its trajectory has already deviated from the precessing common trajectory at a core separation of  $\sim 0.07$  mas (corresponding to a radial distance of  $\sim 15$  pc). Its ejection time is  $t_0 = 1990.0$  (corresponding to  $\phi = 1.77$  rad). The curvature of its trajectory occurs at  $z_1 = z_2 = 2.0$  mas and  $w_1 = w_2 = 0.025$ . This choice of the parameters makes the change of the viewing angle small enough to avoid a large variation of the Doppler boosting. The modeled Lorentz factor is  $\Gamma = \text{const.} = 8.0$ , showing no bulk acceleration. The results of the fitting process are shown in Fig. A.5.

#### 4.4.3. Knot **e**

Knot **e** was not observed when it was within core separation  $\sim 1$  mas, but there is sufficient data sampling beyond this core separation, showing a continuous trajectory curve. As for knot **f** and **a**, we assume that the trajectory of knot **e** has already deviated from the precessing common trajectory at a core separation of  $\sim 0.5$  mas (corresponding to a radial distance of  $\sim 140$  pc to the core). For fitting its kinematics, we take its ejection time  $t_0 = 1996.78$  (BQS17) and the trajectory curvatures occur at  $z_1 = 18$  mas ( $w_1 = -0.008$ ) and  $z_2 = 115$  mas ( $w_2 = 0.020$ ). The modeled Lorentz factor is  $\Gamma = \text{const.} = 21$ , showing no bulk acceleration. The results of the fitting process are shown in Fig. A.6.

#### 4.4.4. Knot **g**

Knot **g** was observed within a core separation of  $\sim 0.5$  mas, but the data points have a complex distribution that is difficult to model. Its ejection time is taken as  $t_0 = 1998.85$  (corresponding to a phase  $\phi = 4.77$  rad; BQS17) and its observed inner trajectory does not follow the precessing nozzle model. We assume that its trajectory has already deviated from the common precessing trajectory at a core separation of  $\sim 0.04$  mas, and it has two curvatures at  $z_1 = 2$  mas ( $w_1 = 0.001$ ) and  $z_2 = 25$  mas ( $w_2 = 0.011$ ), respectively. The first curvature is assumed to occur very near the core in order to avoid the large variation in its flux density due to the variation in the Doppler boosting. The modeled Lorentz factor is  $\Gamma = \text{const.} = 14$ . The results of the fitting process are shown in Fig. A.7.

#### 4.5. Summary

We have performed a model fit to the source kinematics in terms of the precessing nozzle model proposed by Qian et al. (1991, 2014). The model fitting of the kinematics of knots (**c**, **h**, **i**, **j**, **k**), which have regular inner trajectories within core separations of  $\sim 0.3-0.5$  mas<sup>4</sup>, is applied to derive a precessing period of  $\sim 16.9 \pm 0.3$  yr. In Fig. 9 are shown the relation between the modeled ejection (initial) position angle, and the modeled initial viewing angle, and the periodic variations of the ejection position angle and the initial viewing angle with time. These demonstrate that the modeled periodic jet swing spans  $\sim 60^\circ$  and the modeled viewing angle swing spans  $\sim 1.6^\circ$ . The available data only span one period and thus more VLBI monitoring observations in future are needed to test whether or not this regular jet swing behavior is real and continues to occur.

We emphasize that, as explained in Sects. 4.3.1–4.3.6, the precessing period of 16.9 yr was determined with an uncertainty of  $\sim 0.3$  yr. The ejection times modeled for knots **c**, **h**, **i**, **j** and **k** were also determined with an uncertainty of  $\sim 0.3$  yr. Since the model-fitting is based on a specified viewing angle of the jet axis ( $\epsilon = 1.5^\circ$ ), the model-fitting results are not unique.

We found that the entire kinematics of the quasar B1308+326 is complex. The observed kinematic behaviors of knots **f**, **a**, **e** and **g** apparently deviate from the precessing scenario and need to be modeled on the basis of some assumptions: Their inner trajectories (unobserved) could still follow the common trajectory of the precessing nozzle model; and their outer trajectories are explained by introducing trajectory curvatures at core separations of  $\sim 0.3$  mas,  $\sim 0.07$  mas,  $\sim 0.5$  mas and  $\sim 0.04$  mas, respectively<sup>5</sup>.

We have used trajectory curvatures to explain the outer trajectories of knots **c**, **h**, **f**, **a**, **e** and **g**, which deviate from the precessing common trajectory. Referring to Eqs. (23)–(25), we give the parameters  $z_1$ ,  $z_2$ ,  $w_1$  and  $w_2$  in Table 4, in which  $r_1$  and  $r_2$  denote the core separations corresponding to the radial distances  $z_1$  and  $z_2$ . These values indicate that these knots have trajectory curvatures at very different radial distances from  $\sim 16$  pc (knot **g**) to  $\sim 160$  pc (knot **h**).

### 5. Mechanisms of precession

Our results show that the ejection of the superluminal components in the quasar B1308+326 may be quasi-periodic and due to the precession of the jet-nozzle with a period of  $\sim 16.9 \pm 0.3$  yr.

In the literature, several mechanisms have been proposed to explain the precession of jets on parsec-scales in blazars. These may be divided into two categories: the binary-black hole scenario and the single-black hole scenario.

The former category may include three mechanisms:

- Precession due to the orbital motion of a black hole binary. In this case, the jet-launching direction will precess due to the orbital motion of the jet-emitter black hole (Roos 1993; Kun et al. 2015; BQS17).
- Geodetic precession: for a spinning black hole in an orbit about another black hole, its spin and the jet aligned with it will geodetically precess due to the spin-orbit coupling and space curvature (Begelman et al. 1980a, b; Thorne & Blandford 1982; Caproni & Abraham 2004).

<sup>4</sup> The corresponding radial distances (deprojected) are in the range of  $\sim 20-160$  pc.

<sup>5</sup> The corresponding radial distances (deprojected) are  $\sim 9$  mas,  $\sim 2$  mas,  $\sim 18$  mas and  $\sim 2$  mas, respectively.

**Table 4.** Parameters for model-fitting of the outer trajectories of knots *c*, *h*, *f*, *a*, *e* and *g*:  $z_1$ ,  $z_2$ ,  $r_1$ ,  $r_2$ ,  $w_1$  and  $w_2$ .

Knot	$t_0$	$\phi$ (rad)	$z_1$ (mas)	$z_2$ (mas)	$r_1$ (mas)	$r_2$ (mas)	$w_1$	$w_2$
<i>c</i>	1995.54	6.00	18	18	0.8	0.8	0.02	0.02
<i>h</i>	2002.00	3.60	23	23	0.5	0.5	-0.005	-0.005
<i>f</i>	1995.66	5.95	9	40	0.3	1.0	-0.01	0.030
<i>a</i>	1990.00	1.77	2	2	0.074	0.074	0.025	0.025
<i>e</i>	1996.78	5.54	18	115	0.5	3.1	-0.008	0.02
<i>g</i>	1998.85	4.77	2	25	0.036	0.62	0.001	0.011

**Notes.** 1 mas is equivalent to 8.04 pc.

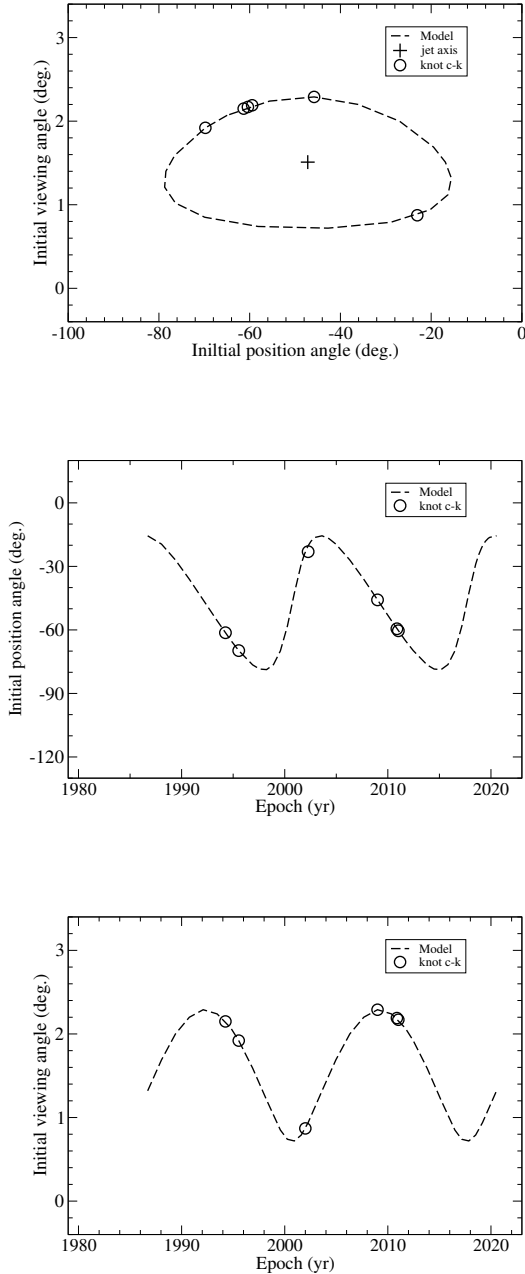


**Fig. 9.** Modeled relations for knots *c*, *d*, *h*, *i*, *j* and *k*. *Top panel:* the ejection position angle versus viewing angle with symbol + denoting the jet axis at  $(-47.2^\circ, 1.5^\circ)$ ; *Middle panel:* the initial position angle swing versus time. *Bottom panel:* the initial viewing angle versus time. All the curves are obtained from the model fitting of the source kinematics in terms of the precession jet nozzle model.

– Newtonian-driven precession: In a binary system, the accretion disk of the primary hole inclined to the orbital plane will precess due to the gravitational torque of the companion hole, leading to the precession of the disk-driven jet (Katz 1997; Britzen et al. 2001; Tateyama & Kingham 2004; Lobanov & Roland 2005; Valtonen & Wiik 2012; Roland et al. 2013, 2015; Valtonen & Pihajoki 2013).

In the latter scenario two mechanisms may be distinguished: (i) spin-induced precession, where the jet associated with an inclined innermost disk is precessed by the central rotating black hole via inertial frame-dragging effect (or Lense-Thirring precession; e.g., Bardeen & Petterson 1975; Scheuer 1992; Scheuer & Feiler 1996; Nelson & Papaloizou 2000; Liu & Melia 2002; Caproni et al. 2004; Qian et al. 2014); or (ii) a jet driven by the innermost disk of a black hole could be precessed by the massive outer disk via an inertial frame-dragging effect (Lense-Thirring effect; Sarazin et al. 1980; Lu 1990).

All possible effects for a binary system are discussed in Sect. 5.2 and for a single black hole in Sect. 5.3.

### 5.1. Binary-black hole scenario

We first discuss the jet precession produced by the motion of a black hole binary and the related gravitational radiation.

#### 5.1.1. Orbital motion

In a black hole binary, the jet-emitter black hole (designated as the primary black hole with mass  $M$ ) moves around the mass center of the system and the orientation of the jet is modulated by its orbital motion due to the composition of the jet-launching velocity and the orbital velocity (cf. Roos et al. 1993; Kun et al. 2015; BQS17).

The period  $T_{\text{orb}}$  of the orbital motion of a binary is given as follows (e.g., Begelman et al. 1980a; Shapiro & Teukolsky 1983; Lang 2002).

$$T_{\text{orb}} = \left[ \frac{4\pi^2 r^3}{G(M+m)} \right]^{\frac{1}{2}} \approx 9.3 \times 10^3 r_{\text{pc}}^{\frac{3}{2}} (M_8 + m_8)^{-\frac{1}{2}} (\text{yr}). \quad (26)$$

Here  $M_8$  and  $m_8$  are the masses of the primary and secondary holes in units of  $10^8 M_\odot$ ,  $r_{\text{pc}}$  is the binary separation in units of parsec,  $G$  is the Newtonian gravitational constant. The separation  $r_{\text{pc}}$  can be written as

$$r_{\text{pc}} \approx 2.4 \times 10^{-3} \left[ \frac{T_{\text{orb}}}{\text{yr}} \right]^{2/3} (M_8 + m_8)^{1/3}. \quad (27)$$

Correspondingly, the post-Newtonian parameter  $\epsilon_0$  is

$$\epsilon_0 = \frac{G(M+m)}{rc^2} \approx 4.8 \times 10^{-6} (M_8 + m_8) / r_{\text{pc}}. \quad (28)$$

The orbital velocity  $v_{\text{orb},M}$  of the primary hole around the center of mass is expressed as

$$v_{\text{orb},M} = \frac{q}{1+q} \sqrt{\frac{G(M+m)}{r}} = \frac{q}{1+q} \left[ \frac{2\pi G(M+m)}{T_{\text{orb}}} \right]^{\frac{1}{3}}. \quad (29)$$

Here  $q = m/M$  is the mass ratio of the binary and thus

$$q = \frac{\beta_{\text{orb},M}}{\epsilon_0^{\frac{1}{2}} - \beta_{\text{orb},M}}. \quad (30)$$

Here  $\beta_{\text{orb},M} = v_{\text{orb},M}/c$ . In order to produce the jet precession of the primary hole, its orbital velocity  $\beta_{\text{orb},M}$  should satisfy the following condition:

$$\tan \eta = \frac{\beta_{\text{orb},M} \sqrt{1 - \cos^2 \omega \sin^2 i}}{\beta_j - \beta_{\text{orb},M} \cos \omega \sin i}. \quad (31)$$

Here  $\beta_j = v_j/c$ ,  $v_j$  is the jet launching velocity,  $c$  is the speed of light,  $\eta$  is the half opening angle of the precession cone,  $i$  is the inclination of the primary disk to the orbital plane (or the angle between the disk axis of the primary hole (jet axis) and the orbital angular momentum), and  $\omega$  is the orbital phase. The numerator of this expression is the orbital velocity component perpendicular to the jet axis (or perpendicular to the disk axis of the primary hole). When angle  $i$  is small or  $\omega \sim 90^\circ$ , this expression can be approximated as:

$$\tan \eta \approx \frac{\beta_{\text{orb},M}}{\beta_j}. \quad (32)$$

Our model-fitting obtains  $T_{\text{orb}} = 8.5$  yr (in the galaxy frame), and  $\eta = 0.79^\circ$ . Taking  $\beta_j \simeq 1$ ,  $i \ll 1$  and  $M_8 + m_8 = 3.6$  (Gupta et al. 2012) and substituting these values into the formulas given above, we can obtain the values of parameters  $M_8$ ,  $m_8$ ,  $q$  and  $\beta_{\text{obs},M}$ , which are listed in Table 5. It can be seen that the hole separation  $r \simeq 1.5 \times 10^3 r_g$  ( $r_g$  – the gravitational radius of the primary hole). If the radius of the primary hole disk is of the order of  $\sim 60 r_g$ , within which the jet is formed, then the derived hole separation seems large enough ( $\sim 25$  times the radius of the disk) to assure that the primary disk and its associated jet are stable under the gravitational effects of the secondary hole<sup>6</sup>. In addition, here we obtain a relatively large mass ratio  $q \sim 0.70$  for B1308+326.

### 5.1.2. Gravitational radiation

Luminous quasars are believed to harbor supermassive black holes that provide their powerful radiation sources. Specifically, for example, blazar OJ287 displays a periodic optical variability of  $\sim 12$  yr, and has been interpreted as being a Keplerian binary with evidence of orbital decay by emission of gravitational waves (Valtonen et al. 2006a,b, 2008, 2010, 2011).

As we have shown above, the periodic ejection of superluminal components (or the jet swing) observed in B1308+326 could be interpreted in terms of the orbital motion of a putative supermassive black hole binary in its nucleus. According to general relativity (Einstein 1916, 1918), two black holes in orbit will spiral together due to the loss of energy and momentum through gravitational radiation. Coalescence of a supermassive black hole binary comprises three phases: inspiral, merger,

**Table 5.** Model parameters for the mechanism of orbital motion of a black hole binary.

Parameter	B1308+326
$z$	0.997
$M_8$	2.12
$m_8$	1.48
$q$	0.7
$r(\text{pc})$	0.015
$\epsilon_0$	0.0011
$\eta(\text{deg})$	0.79
$\beta_{\text{obs},M}$	0.0138

and ringdown, all of which are processes emitting gravitational waves. For B1308+326, the binary separation is estimated to be  $\sim 0.015$  pc and the post-Newtonian parameter  $\epsilon_0 \sim 1.2 \times 10^{-3}$ . Thus, it should have started to enter the inspiral phase with the energy-momentum loss by gravitational radiation dominating the shrinkage of the orbit before ultimate merging (Haehnelt 1994; Volonteri et al. 2003). We can estimate the parameters of gravitational radiation as follows (cf. Peters 1964; Misner et al. 1973; Thorne & Braginsky 1976; Shapiro & Teukolsky 1983; Fukushige & Ebisuzaki 1992; Kokkotas & Schmidt 1999; Gergely & Biermann 2009; Amaro-Seoane & Santamaria 2010).

During the inspiral phase of a black hole binary system, the gravitational radiation lifetime  $t_{\text{gr}}$ , and the luminosity  $L_{\text{gr}}$  and frequency  $f_{\text{gr}}$  of the gravitational waves can be calculated as:

$$t_{\text{gr}} = \frac{5}{256} \frac{c^5}{G^3} \frac{r^4}{mM(m+M)}, \quad (33)$$

or

$$t_{\text{gr}} \simeq 5.7 \times 10^{14} \frac{r_{\text{pc}}^4}{m_8 M_8 (M_8 + m_8)} \text{ (yr)}, \quad (34)$$

and

$$L_{\text{gr}} = \frac{32}{5} \frac{G^4}{c^5} \frac{m^2 M^2 (M+m)}{r^5}, \quad (35)$$

or

$$L_{\text{gr}} \simeq 6.0 \times 10^{33} \frac{m_8^2 M_8^2 (M_8 + m_8)}{r_{\text{pc}}^5} \text{ (erg s}^{-1}\text{)}, \quad (36)$$

and

$$f_{\text{gr}} = \frac{2(1+z)}{T_p}, \quad (37)$$

or

$$f_{\text{gr}} \simeq 6.3 \times 10^{-8} (1+z) / T_{p,\text{yr}} \text{ (Hz)}. \quad (38)$$

When a binary coalesces, the gravitational wave period  $P_{\text{gw}}$  and the dimensionless amplitude  $h_{\text{gw}}$  can be estimated as:

$$P_{\text{gw}} = \frac{3\sqrt{3}\pi G}{c^3} (m+M)(1+z), \quad (39)$$

or

$$P_{\text{gw}} \simeq 8.1 \times 10^3 (m_8 + M_8)(1+z) \text{ (s)}. \quad (40)$$

The gravitational wave frequency  $f_{\text{gw}} = 1/P_{\text{gw}}$ .

$$h_{\text{gw}} = \left(6\sqrt{3}\pi k\right)^{\frac{1}{2}} \frac{G(M+m)}{D_L c^2}, \quad (41)$$

<sup>6</sup> In this paper, we assume  $q < 1$ ; the mass of the jet-producing supermassive black hole is larger than the mass of the companion,  $M > m$ . Otherwise we have to explain why the smaller hole has a jet, and the larger hole does not.

**Table 6.** Parameters of gravitational radiation for B1308+326.

Parameter	B1308+326
$t_{\text{gr}}(\text{yr})$	$2.6 \times 10^6$
$f_{\text{gr}}(\text{Hz})$	$7.4 \times 10^{-9}$
$L_{\text{gr}}(\text{erg s}^{-1})$	$2.8 \times 10^{44}$
$P_{\text{gw}}(\text{s})$	$5.8 \times 10^4$
$f_{\text{gw}}(\text{Hz})$	$1.7 \times 10^{-5}$
$h_{\text{gw}}$	$3.2 \times 10^{-15}$

**Notes.** The gravitational radiation lifetime  $t_{\text{gr}}$ , frequency  $f_{\text{gr}}$  and luminosity  $L_{\text{gr}}$  during the inspiral regime. The gravitational wave period  $P_{\text{gw}}$ , frequency  $f_{\text{gw}}$  and dimensionless amplitude  $h_{\text{gw}}$  when it coalesces.

or

$$h_{\text{gw}} \simeq 6.1 \times 10^{-15} \left( \frac{k}{0.05} \right)^{\frac{1}{2}} \left( \frac{D_L}{Gpc} \right)^{-1} (m_8 + M_8). \quad (42)$$

Here  $k$  is the emission efficiency of the gravitational radiation. For the massive stellar binary black hole merger GW20150914 observed by Laser Interferometer Gravitational-Wave Observatory (*LIGO*),  $k \simeq 0.046$  (Abbott et al. 2016b). We list the relevant values for the putative black hole binary in the quasar B1308+326 in Table 6. It can be seen that during its inspiral phase, the frequency of emitted gravitational waves is of the order of  $10^{-8}$  Hz, which is too low to be detected by currently planned gravitational detectors (e.g., European Laser Interferometer Space Antenna, *eLISA*). However, when it coalesces, the frequency of gravitational wave could reach the lower end ( $\sim 10^{-5}$  Hz) of gravitational detectors such as *LISA* (Jafry et al. 1994; Artymowicz 1998; Bender 1998; Bender & Dieter 2003; Komossa 2003; Merritt 2003; Milosavljevic & Merritt 2003; Merritt & Milosavljevic 2005; Sesana et al. 2009; Amaro-Seoane et al. 2013; Fariss et al. 2014; Bogdanovic 2015).

Recently, Valtonen et al. (2016) observed the predicted optical outburst in OJ287 occurring in November–December 2015, which is clearly separated into thermal bremsstrahlung and synchrotron components. With its thermal bremsstrahlung lasting only for about two weeks, the key issue on the radiation mechanisms of the outbursts (Qian 2015) is solved. This confirms the applicability of their binary black hole model and implies that in the case of OJ287, evidence for gravitational radiation during the inspiral phase can be inferred from the modeling of the orbital precession and timing of the quasi-periodic optical outbursts (Valtonen et al. 2008). In general, coalescence of supermassive ( $\sim 10^8 M_{\odot}$ ) black hole binaries would constitute the strongest sources of gravitational waves, but at very low frequencies in the range  $10^{-6}$ – $10^{-8}$  Hz. Different techniques for detection of these gravitational waves would be required (e.g., pulsar-timing technique; Sesana et al. 2009). The recent discovery of the gravitational wave source GW150914 with the Advanced *LIGO* detectors (Abbott et al. 2016a–d; Castevecchi 2016) demonstrates a very bright future for detecting gravitational waves in extragalactic black hole binaries, possibly including some nearby blazars with very short precession periods.

### 5.1.3. Geodetic precession

We consider the geodetic precession (or spin-orbit precession) mechanism, in which the gravitational torque induced by the orbiting secondary hole causes the precession of the inner disk

of the spinning primary hole (Begelman et al. 1980a; Thorne & Blandford 1982). The precession period can be expressed as (Begelman & Sarazin 1980b):

$$T_{\text{geo}} = \frac{\pi c^2 r^{\frac{5}{2}} (m + M)^{\frac{1}{2}}}{G^{\frac{3}{2}} m M} \left( 1 + \frac{3}{4} \frac{m}{M} \right)^{-1}, \quad (43)$$

or

$$T_{\text{geo}} \simeq 1.0 \times r_{\text{pc}}^{\frac{5}{2}} \frac{(m_8 + M_8)^{\frac{1}{2}}}{m_8 M_8} \left( 1 + \frac{3}{4} q \right)^{-1} (\text{yr}). \quad (44)$$

For B1308+326,  $T_{\text{geo}} \simeq 1.2 \times 10^4$  yr, which is too long to be relevant to the observed periodic ejection of its superluminal components, but might be used to understand the possible existence of jet precession on 1–100 kpc scales in the source (Cassaró et al. 2002; BQS17).

### 5.1.4. Newtonian-driven precession

Now we come to consider the Newtonian-driven precession (the precessing disk model proposed by Katz 1997), in which the gravitational torque of the orbiting secondary hole on the inclined primary disk causes the precession of the primary disk and the associated jet. The primary disk will precess at a rate:

$$T_{\text{prec}} = \frac{8\pi}{3} \frac{r^3}{(GM)^{\frac{1}{2}} r_d^{\frac{3}{2}} \cos \theta_0}. \quad (45)$$

$\theta_0$  is the inclination of the primary disk to the orbital plane and  $r_d$  is the radius of the disk (e.g., Katz 1997; Romero et al. 2000; Tateyama & Kingham 2004).

Using the relation between the orbital period  $T_{\text{orb}}$  and the orbital separation  $r$  (Eq. (26) or (27)) we can express the radius of the primary disk  $r_{d,M}$  as:

$$r_{d,M} \simeq 2.7 \times 10^{-3} \left[ \frac{T_{\text{orb}}^2 (M_8 + m_8) \sqrt{M_8}}{T_{\text{prec}} m_8 \cos \theta_0} \right]^{\frac{2}{3}}, \quad (46)$$

or

$$\frac{r_{d,M}}{r_{\text{orb}}} \simeq 1.1 \left( \frac{T_{\text{orb}}}{T_{\text{prec}}} \right)^{\frac{2}{3}} (\sec \theta_0)^{\frac{2}{3}} \left( \frac{1+q}{q^2} \right)^{\frac{1}{3}}. \quad (47)$$

Here,  $r_{d,M}$  and  $r_{\text{orb}}$  are in units of parsec, and  $T_{\text{orb}}$  and  $T_{\text{prec}}$  are in years.

Assuming that the periodic jet swing observed in B1308+326 is due to the Newtonian-driven precession mechanism ( $T_{\text{prec}} = 8.5$  yr) and that the ratio between the precession period and the orbital period is  $T_{\text{prec}}/T_{\text{orb}} \simeq 5$ , which might be regarded as the lowest limit for binary hole systems (see Priedhorsky & Holt 1987; Wijnands et al. 1996; Katz 1997), we then obtain a relatively short orbital period  $T_{\text{orb}} \simeq 1.7$  yr (in the galaxy frame). Substituting the total mass of the binary black hole ( $M_8 + m_8 = 3.6$ ) and this  $T_{\text{orb}}$  into Eq. (27), we can estimate the binary separation  $r \simeq 0.0052$  pc. We can also estimate the primary disk radius  $r_{d,M}$  from Eq. (46) ( $\theta_0 = \eta = 0.79^\circ$ ), yielding  $r_{d,M} \simeq 0.0092$  pc. This indicates that the primary disk radius is larger than the binary separation, and that the orbiting secondary hole will impact and cross the primary disk twice every  $\sim 1.7$  yr ( $\sim 3.4$  yr in the observer's frame). In this case, the primary disk and its associated jet might be extremely unstable under the strong gravitational influences from the companion, except the mass ratio is very small<sup>7</sup>. Therefore the precessing disk

<sup>7</sup> For OJ287, the secondary hole impacts the primary disk twice every  $\sim 9.2$  yr (in the source frame) and the mass ratio is only  $\sim 10^{-2}$  (Valtonen & Wiik 2012).

model due to a Newtonian-driven precession mechanism seems unable to explain the periodic jet swing observed in B1308+326.

In addition, we note that the Newtonian precession mechanism has been applied to explain the jet precession in blazar OJ287 (Katz 1997; Valtonen & Wiik 2012). However, in the case of OJ287, the inclination of the primary disk to the orbital plane is large ( $>50^\circ$ – $90^\circ$ ), and the Doppler boosting is narrowly peaked around its maximum when the jet points nearly directly toward the observer, that is, Doppler beaming effects will not appear during most of the precession period. This is in contradiction to the observations in the radio, optical, and  $\gamma$ -ray bands. These observations reveal that Doppler-boosted flares occur during the whole precession period. For example, the two radio-optical- $\gamma$ -ray bursts observed in 2008 October and 2009 October (Agudo et al. 2011) occurred between the two optical peaks in 2005/2006 and 2015/2016 produced by the jet precession. Therefore, we would think that the Newtonian-driven disk precession mechanism does not seem applicable to OJ287 either.

In summary, among the three mechanisms producing precession in the binary black hole scenario (orbital motion, geodetic precession and Newtonian-driven precession), the orbital motion of the putative supermassive black hole binary may be the most likely mechanism for the jet precession in B1308+326.

### 5.1.5. Multiple precession

Above we discussed the plausible jet-precession mechanisms for the periodic ejection of the superluminal components in the quasar B1308+326 under the binary black hole scenario. Usually, jet precession is directly observed in radio quasars, especially in blazars on parsec-scales, because their jets closely direct toward us and are Doppler boosted. Generic radio quasars and radio galaxies have their jets directing with larger angles relative to the line of sight and their radio structures consist of cores, jets, and lobes (with hotspots) of sizes ranging from pc to 100 kpc scales (e.g., in Cygnus A, Hargrave & Ryle 1974; Perley et al. 1984), even to  $\sim 1$  Mpc in some giant radio galaxies (e.g., in DA240, Tsien 1982; Tsien & Saunders 1982). In radio quasars and radio galaxies, jet precession on kpc to 100 kpc scales has been detected (e.g., Gower et al. 1982). Therefore, it can be seen that jet precession may have different timescales ranging from a few years to  $\sim 10^{4-6}$  yr. Multi-precession may exist simultaneously in blazars and radio quasars/galaxies due to different mechanisms, if the binary scenario is applicable. There are at least four mechanisms that could be at play: (i) orbital motion; (ii) Newtonian gravitational torque on disk; (iii) geodetic precession; and (iv) Kerr hole's Lense-Thirring effect (see below). For B1308+326, the comparison of the 1.46GHz VLA-image (Cassaró et al. 1999) with the 15 GHz VLBI-images seems to reveal some evidence for both pc-scale and kpc-scale jet swings (BQS17).

## 5.2. Single black hole scenario: Lense-Thirring precession

Now, we come to consider the single supermassive black hole scenario.

Since the precession period of an inner disk driven by the massive outer disk through Lense-Thirring effect is of the order of  $\sim 10^4$  yr (Lu et al. 1990), this precession mechanism can not be used to explain the periodic jet swing observed in B1308+326.

The spin-induced precession may be an important mechanism for interpreting the periodic variability in optical/radio light

curves and the periodic ejection of superluminal components in blazars. Based on the Bardeen-Peterson effect, the torque of a rotating black hole on its tilted accretion disk (due to the frame-dragging effect) can cause a global precession of the accretion disk and the associated jet. This mechanism has been applied to several blazars (Lense & Thirring 1918; Bardeen & Peterson 1975; Scheuer 1992; Scheuer & Feiler 1996; Nelson & Papaloizou 2000; Liu & Melia 2002; Caproni et al. 2004; Qian et al. 2014). Here, strong viscosity and/or magnetic coupling are required so that the jet-forming disk regions are operated by the Lense-Thirring effect (Fragile 2007; Nixon & King 2013).

Some general relativistic MHD simulations for an accretion disk misaligned with respect to the spin axis of a Kerr black hole have shown that there seems to be a lack of indication of the alignment of the inner disk with the spin axis caused by the Bardeen-Peterson effect, but the global precession of the main inner-disk is confirmed (e.g., Fragile et al. 2007; Zhuravlev et al. 2015). Thus, if this mechanism could be used to interpret the precession of jets, some information about the size of jet-forming disk regions and the relation between the precession period and the ratio  $M/j$  ( $M$  – mass of the black hole and  $j$  – dimensionless spin parameter, see below) could be obtained. The VLBI observations of radio galaxy M 87 at mm wavelengths (7 mm, 3.5 mm and 1.3 mm: e.g., Ly et al. 2007; Hada et al. 2011; Asada & Nakamura 2012; Dexter et al. 2012; Dolemann et al. 2012; Hada et al. 2012; Krichbaum et al. 2014) have reached its horizon-scale structure and provided some significant information about the scales on which the jet is formed. It was found that the width of its mm-core follows a power-law as a function of the distance to the origin of the jet, which is close to the hole-horizon. The width of the 1.3 mm core (Doeleman et al. 2012) is  $\sim 11 \pm 0.8 r_g$  ( $r_g$  – the gravitational radius and the mass of its hole  $M = 6.4 \times 10^9 M_\odot$ ; Gebhardt & Thomas 2009; Gebhardt 2011). Taking this 1.3 mm core width as the size of the jet-base, and considering the diameter of the innermost stable circular orbit (ISCO) magnified by the lensing effects of the Kerr spacetime metric near the rotating black hole, the spin of the black hole in M 87 was estimated to be  $j \sim 0.6$  by Doeleman et al. (2012) ( $j = J/J_{\max}$  – the dimensionless spin parameter,  $J$  – the angular momentum and  $J_{\max} = GM^2/c$  – the maximum angular momentum)<sup>8</sup>.

In blazars, the relativistic jets are closely aligned to the line of sight and mm-VLBI observations cannot provide any information about the location and size of their jet-bases. However, Marscher et al. (2008) used the rotation rate of the optical polarization angle during an optical flare observed in BL Lacertae combined with the 7-mm VLBI monitoring of the kinematics of the superluminal components to infer the size of the jet-base. They found that the outer edge (or the outer magnetic field line) of the jet is anchored in the accretion disk at  $\sim 60 r_g$  (assuming  $M_H = 2 \times 10^8 M_\odot$ ). Thus, the jet in BL Lacertae is suggested to be driven by the twisting magnetic fields from the vicinity of an accreting black hole. The Newtonian-driven precession mechanism seems unable to explain periodic jet swings with periods of the order of  $\sim 10$  yr. For example, Caproni et al. (2013) showed that in order to explain the jet nozzle precession of BL Lacertae in terms of the Newtonian-driven mechanism, the mass of the secondary hole should be much larger than the jet-producing primary hole.

Referring to the observational and theoretical results for M 87 and BL Lacertae, it is possible to explain the jet-nozzle precession observed in B1308+326 in terms of the Lense-Thirring effect of the putative central rotating black hole on its inner disk.

<sup>8</sup> The lower limit ( $3\sigma$ ) is  $j = 0.2$ , see Doeleman et al. (2012).

**Table 7.** The relation between the inner radius ( $\bar{r}_{\text{inn}} = r_{\text{inn}}/r_g$ ) and outer radius ( $\bar{r}_{\text{out}} = r_{\text{out}}/r_g$ ) of the precessed disk and the Kerr hole’s spin  $j$ .

$j$	$\bar{r}_{\text{inn}}$	$\bar{r}_{\text{out}}$
0.10	5.7	32
0.20	4.9	45
0.40	4.6	63
0.60	3.8	78
0.80	2.9	95
0.90	2.3	106
0.95	1.9	113

Assuming a standard thin disk model (e.g., Shakura & Sunyaev 1973) with a constant surface density and a rigid disk precession (Bardeen & Peterson 1975; Nelson & Papaloizou 2000), the spin-induced precession period can be approximately written as (Liu & Melia 2002; Caproni et al. 2004; Fragile et al. 2007; Qian et al. 2014; Zhuravlev et al. 2015):

$$P_{\text{prec}}(\text{yr}) \simeq (9.82 \times 10^{-5}) \frac{M_9}{j} \bar{r}_{\text{out}}^{5/2} f(\bar{r}_{\text{inn}}, \bar{r}_{\text{out}}), \quad (48)$$

$$f(\bar{r}_{\text{inn}}, \bar{r}_{\text{out}}) = \bar{r}_{\text{inn}}^{1/2} \frac{1 - \left(\frac{\bar{r}_{\text{inn}}}{\bar{r}_{\text{out}}}\right)^{5/2}}{1 - \left(\frac{\bar{r}_{\text{inn}}}{\bar{r}_{\text{out}}}\right)^{1/2}}. \quad (49)$$

Where  $M_9$  is the mass of the spinning black hole in units of  $10^9$  solar mass ( $M_9 = M_{\text{BH}}/10^9 M_\odot$ ), and  $\bar{r}_{\text{out}} = r_{\text{out}}/r_g$ ,  $\bar{r}_{\text{inn}} = r_{\text{inn}}/r_g$  are the inner and outer radii of the precessed disk region in which the jet is anchored.

As usual, we assume that the inner radius is equivalent to the innermost stable circular orbit radius  $r_{\text{ISCO}}$ , which depends on the spin of a Kerr black hole as follows:

$$r_{\text{ISCO}} = r_g \left[ 3 + Z_2 - \sqrt{(3 - Z_1)(3 + Z_1 + 2Z_2)} \right], \quad (50)$$

where

$$Z_1 = 1 + (1 - j)^{1/3} \left[ (1 + j)^{1/3} + (1 - j)^{1/3} \right], \quad (51)$$

$$Z_2 = (3j^2 + Z_1^2)^{1/2}. \quad (52)$$

For B1308+326,  $M_9 = 0.36$ , and  $P_{\text{prec}} = 8.5$  yr, the relation between the inner and outer radii of the precessed disk and the spin  $j$  of the primary hole can be estimated and is given in Table 7. If the outer footpoint of the jet is anchored at  $\sim 50$ – $60 r_g$  as suggested by Marscher et al. (2008) for BL Lacertae, then the spin of the quasar B1308+326 is  $j \simeq 0.2$ – $0.4$ .

## 6. Summary and discussion

We have investigated the kinematics of the superluminal components in the quasar B1308+326 and found that the change of the ejection position angle of the superluminal knots might be regular and quasi-periodic due to its jet nozzle precession. The modeling results are only preliminary and not unique, but might be useful for understanding the physics of blazars. This quasi-periodic jet swing might be worth searching for in the future VLBI observations with sufficient data sampling on sub-parsec scales.

As discussed in Sect. 5, our analysis shows that the precession of the jet-nozzle in the quasar B1308+326 may plausibly be induced by two mechanisms: The orbital motion of the jet-producing black hole in a binary system, and the Lense-Thirring effect of a rotating (Kerr) supermassive black hole on

its accretion-disk. Other mechanisms seem to be ruled out, because they cannot explain its short precession period of 8.5 yr (in the source frame). At present, there seems no critical arguments which could discriminate between the two mechanisms. We might speculate that the jet precession due to the orbital motion might be able to last many periods, such as in OJ287, while the jet precession induced by the Lense-Thirring effect might be unable to last many periods, because this mechanism may depend on the strongly variable mass/field accretion of the black hole/accretion disk system. More VLBI monitorings with highest resolutions and studies of correlations between optical and radio variations would be very helpful for solving this issue.

The formation of relativistic jets has been studied in the literature by many authors working on relativistic magnetodynamics for the formation-collimation-acceleration of relativistic jets in blazars (e.g., Blandford & Znajek 1977; Blandford & Payne 1982; Camenzind 1987, 1990; Punsly & Coroniti 1990; Chieuh et al. 1991; Li et al. 1992; Beskin 1997, 2010; Fendt 1997; Ghosh & Abramowicz 1997; Meier 1999, 2013; Liu & Melia 2002; Vlahakis & Königl 2004; Caproni 2006; Vlahakis 2006; Komissarov et al. 2007; Tchekhovskoy et al. 2010). According to these theories, relativistic jets can be produced by a highly magnetized rotating accretion disk and/or a rotating black hole/ergosphere. Thus, relativistic jets could have stratified structures (e.g., a core-spine-sheath structure), comprised of a few components driven from different regions: for example, the rotating black hole horizon-driven component (Blandford & Znajek 1977); the ergo-disk driven component (Punsly & Coroniti 1990; Meier 1999, 2013); and the innermost disk driven component and disk driven winds (Camenzind 1987, 1990; Camenzind & Krockenberger 1992). The formation of precessing nozzle may be mainly related to the processes in the former three regions around rapidly rotating black holes.

Precessing jet nozzle models have been applied to explain the periodic jet position angle swings and periodic changes in ejection angle of superluminal components and their kinematics on parsec-scales in several blazars (cf. Introduction). Thus, periodic (or quasi-periodic) ejection of superluminal components from a precessing nozzle might be a common phenomenon in blazars at least during some stable periods of these sources.

Our precessing nozzle scenario consists of two ingredients: The ejection of superluminal components by a precessing nozzle and the jet features moving along an apparently common precessing trajectory in the innermost core separations ( $< 0.3$ – $0.5$  mas). These ingredients could be understood in terms of the theory of relativistic magnetohydrodynamics for the formation/collimation/acceleration of relativistic jets in blazars. The structure of the jets observed in the radio galaxy M 87 (parabolic hollow jet nozzle structure; Nakamura & Asada 2013) and in OJ287 (“fork”-like jet structure; Tateyama 2013) might be regarded as evidence.

It has been suggested that magnetic nozzles can be formed in disk-driven jets in the magnetospheres of rotating black hole/accretion disk systems. These are located near the classical fast magnetosonic point, where the magnetohydrodynamic flow remains Poynting flux dominated. In self-similar axisymmetric MHD flow models, beyond the classical fast magnetosonic point, the jet will be accelerated until approaching the modified fast magnetosonic point (Blandford & Znajek 1977; Li et al. 1992; Vlahakis & Königl 2004). This extended acceleration is due to the dominance of Poynting flux at the classical magnetosonic point, thus having ample electromagnetic energy to be transformed to plasma kinetic energy (Komissarov et al. 2007; Komissarov 2009; Millas et al. 2014). In the case of relativistic

jets, the classical fast magnetosonic point is located in the force-free region of the magnetosphere where the magnetic energy dominates the plasma kinetic energy. The magnetic field lines anchored into the innermost disk and the magnetic nozzle would rotate rigidly with the disk (MacDonald & Throne 1982).

Additionally, according to the relativistic MHD theories for relativistic jets, beyond the magnetic nozzle (or beyond the classical fast magnetosonic point), the jet will be greatly accelerated until approaching the modified fast magnetosonic point via the transformation of electromagnetic energy into plasma kinetic energy. In this extended acceleration region, the inertia of the plasma becomes strong and the electromagnetic fields are neither degenerate nor force free, and the plasma will flow along its own streamlines. As generally studied, in the case of axis-symmetric (steady) black hole/disk magnetosphere, the streamlines of the plasma flows are axisymmetric. Thus, the components ejected from the magnetic nozzle at different epochs would follow self-similar trajectories, lightening their own streamlines and creating their own magnetic channels<sup>9</sup>. This may explain why the superluminal knots observed by VLBI move along a precessing common trajectory; a precessing helical trajectory (e.g., in 3C 345 and NRAO 150) or a precessing ballistic trajectory (e.g., in 3C 454.3, 3C 279 and B1308+326).

In recent years general relativistic MHD simulations of relativistic jet formation near a Kerr black hole have shown some significant properties of this process, demonstrating the dependence of the jet formation on the mass accretion, magnetic field, and the spin of the hole. In particular, these simulations show that the evolution of the jet formation may undergo a few stages related to different states of the mass/field accretion onto the black hole. For example, in the framework of the magnetic arrested disk (MAD) scenario (Dexter et al. 2014; Narayan et al. 2014; Tchekhovskoy 2014; McKinney et al. 2015), the evolution process of the jet could follow five stages, closely depending on the evolution of the accretion of mass and magnetic field: Disk-aligned jet with Lense-Thirring precession  $\Rightarrow$  spin-aligned jet with erratic wobbling  $\Rightarrow$  steady spin-aligned jet  $\Rightarrow$  no jet (pure compact core)  $\Rightarrow$  jet revival. The phenomenon observed in B1308+326 (from compact core  $\Rightarrow$  precessing jet  $\Rightarrow$  compact core  $\Rightarrow$  jet revival) might be regarded as an example predicted by such a MAD-scenario. Moreover, The alternative occurrence of Lense-Thirring precession and erratic wobbling predicted by the MAD-mechanism might explain why we have not observed long-term jet precession lasting for decades in blazars. This situation might be mostly associated with the variations of the direction of accreted magnetic fields, which change the jet formation processes. In addition, Zamaninasab et al. (2014) reported that, for blazars and radio galaxies, the accretion disk luminosity is tightly correlated with the jet magnetic field, implying that strong magnetic fields exist in the vicinity of the black holes and providing direct evidence for jets produced via the Blandford-Znajek mechanism (Blandford & Znajek 1977).

In summary, we have shown that the precessing nozzle model could explain the quasi-periodic ejection of superluminal components, jet position angle swing, and parsec-scale kinematics of the superluminal components observed in the bright quasar B1308+326. This model has a theoretical basis and can be understood in terms of the theories of relativistic magnetohydrodynamics for relativistic jets.

*Acknowledgements.* We have used the MOJAVE database to model the VLBI maps of B1308+326. The database is maintained by the MOJAVE team (Lister et al. 2009).

## References

- Abraham, Z., & Romero, G. E. 1999, *A&A*, 344, 61  
 Abbott, B. P., Abbott, R., Abbott, T. D., et al. 2016a, *Phys. Rev. D*, 93, 122003  
 Abbott, B. P., Abbott, R., Abbott, T. D., et al. 2016b, *ApJ*, 833, L1  
 Abbott, B. P., Abbott, R., Abbott, T. D., et al. 2016c, *ApJ*, 818, L22  
 Abbott, B. P., Abbott, R., Abbott, T. D., et al. 2016d, *Phys. Rev. Lett.*, 116, 061102  
 Acero, F., Ackermann, M., Ajello, M., et al. 2015, *ApJS*, 218, 23  
 Ackermann, M., Ajello, M., Allafort, A., et al. 2011, *ApJ*, 743, 171  
 Ackermann, M., Ajello, M., Allafort, A., et al. 2013, *ApJS*, 209, 34  
 Agudo, I. 2009, in *Approaching Micro-Arcsecond Resolution with VSOP-2: Astrophysics and Technology (ASPCS 402)*, eds. Y. Hagiwara, E. Fomalont, H. Tsuboi, & Y. Murata, 330  
 Agudo, I., Bach, U., Krichbaum, T. P., et al. 2007, *A&A*, 476, L17  
 Agudo, I., Jorstad, S. J., Marscher, A. P., et al. 2011, *ApJ*, 726, L13  
 Amaro-Seoane, P., & Santamaria, L. 2010, *ApJ*, 722, 1197  
 Amaro-Seoane, P., Aoudia, S., Babak, S., et al. 2013, *GW Notes*, 6, 4  
 Angel, J. R. P., & Stockman, H. S. 1980, *ARA&A*, 18, 321  
 Artymowicz, P. 1998, in *Theory of Black Hole Accretion Disks*, eds. M. A. Abramowicz, G. Bjornsson, & J. E. Pringle (Cambridge Univ. Press), 202  
 Asada, K., & Nakamura, M. 2012, *ApJ*, 745, L28  
 Bardeen, J. M., & Petterson, J. A. 1975, *ApJ*, 195, L65  
 Begelman, M. C., Blandford, R. D., & Rees, M. J. 1980a, *Nature*, 287, 307  
 Begelman, M. C., Sarazin, C. L., Hatchett, S. P., et al. 1980b, *ApJ*, 238, 722  
 Bender, P. L. 1998, in *Eighteenth Texas Symposium on Relativistic Astrophysics and Cosmology*, eds. A. V. Olinto, J. A. Frieman, & D. N. Schramm, 536  
 Bender, P. L., & Dieter, H. 2003, *Adv. Space Res.*, 32, 1243  
 Beskin, V. S. 1997, *Physics-Uzpekhi*, 40, 659  
 Beskin, V. S. 2010, *Physics-Uzpekhi*, 53, 1199  
 Beskin, V. S., & Zheltoukhov, A. A. 2013, *Astron. Lett.*, 39, 215  
 Biretta, J. A., Junor, W., & Livio, M. 2002, *New Astron. Rev.*, 46, 239  
 Blandford, R. D., & Payne, D. G. 1982, *MNRAS*, 199, 883  
 Blandford, R. D., & Znajek, R. L. 1977, *MNRAS*, 179, 433  
 Bogdanovic, T. 2015, *Astrophysics and Space Science Proceedings*, 40, 103  
 Britzen, S., Roland, J., Laskar, J., et al. 2001, *A&A*, 374, 784  
 Britzen, S., Qian, S. J., Steffen, W., et al. 2017, *A&A*, 602, A29 (BQS17)  
 Calzadilla, M., Fish, V. L., Lu, R., et al. 2015, *AAS Meeting*, 225, 432.11  
 Camenzind, M. 1987, *A&A*, 184, 341  
 Camenzind, M. 1990, in *Galactic and Intergalactic Magnetic Fields, Proceedings of the 140th Symposium of IAU*, 413  
 Camenzind, M., & Krockenberger, M. 1992, *A&A*, 255, 59  
 Caproni, A., & Abraham, Z. 2004, *ApJ*, 602, 625  
 Caproni, A., Cuesta, H. J. M., & Abraham, Z. 2004, *ApJ*, 616, L99  
 Caproni, A., Livio, M., Abraham, Z., & Cuesta, H. J. M. 2006, *ApJ*, 653, 112  
 Caproni, A., Abraham, Z., & Monteiro, H. 2013, *MNRAS*, 428, 280  
 Carrasco, L., Escobedo, G., Mayya, D. Y., et al. 2012, *ATel*, 4234  
 Cassaro, P., Stanghellini, C., Bondi, M., et al. 1999, *A&AS*, 139, 601  
 Cassaro, P., Stanghellini, C., Dallacasa, D., et al. 2002, *A&A*, 381, 378  
 Castelletti, D. 2016, *Nature*, 530, 261  
 Chieuh, Z. H., Li, Z. Y., & Begelman, M. C. 1991, *ApJ*, 377, 462  
 Dexter, J., McKinney, J. C., & Agol, E. 2012, *MNRAS*, 421, 1517  
 Dexter, J., McKinney, J. C., Markoff, S., & Tchekhovskoy, A. 2014, *MNRAS*, 440, 2185  
 Dhawan, V., Kellerman, K. I., & Romney, J. D. 1998, *ApJ*, 498, L111  
 Doleman, S. S., Fish, V. L., Schenck, D. E., et al. 2012, *Science*, 338, 355  
 Einstein, A. 1916, *Sitzungsberichte der Königlich Preussischen Akademie der Wissenschaften (SPAW, Berlin)*, 688  
 Einstein, A. 1918, *Sitzungsberichte der Königlich Preussischen Akademie der Wissenschaften (SPAW, Berlin)*, 154  
 Farris, B. D., Duffell, P., MacFadyen, A. I., et al. 2014, *ApJ*, 783, 134  
 Fendt, C. 1997, *A&A*, 319, 1025  
 Fragile, P. C., Blaes, O. M., Anninos, P., & Salmonson, J. D. 2007, *ApJ*, 668, 417  
 Fukushima, T., & Ebisuzaki, T. 1992, *ApJ*, 396, L61  
 Gebhardt, K., & Thomas, J. 2009, *ApJ*, 700, 1690  
 Gebhardt, K., Adams, J., Richstone, D., et al. 2011, *ApJ*, 729, 119  
 Gergely, L. A., & Biermann, P. L. 2009, *ApJ*, 697, 1261  
 Ghosh, P., & Abramowicz, M. A. 1997, *MNRAS*, 292, 887  
 Gower, A. C., Gregory, P. C., Unruh, W. G., & Hutchings, J. B. 1982, *ApJ*, 262, 478  
 Graham, M. J., Djorgovski, S. G., Stern, D., et al. 2015, *Nature*, 518, 74  
 Gupta, S. P., Pandey, U. S., Singh, K., et al. 2012, *New Astron.*, 17, 8  
 Hada, K., Doi, A., Kino, M., et al. 2011, *Nature*, 477, 185

<sup>9</sup> The precession of a jet nozzle with ballistically moving superluminal knots implies that these knots are moving along their own field tubes, not along a precessing common magnetic tube.

- Hada, K., Kino, M., Nagai, H., et al. 2012, *ApJ*, **760**, 562
- Haehnelt, M. G. 1994, in *Multi-Wavelength Continuum Emission of AGN*, eds. T. J.-L. Courvoisier, & A. Blecha, 279
- Hardee, P. E. 1987, *ApJ*, **318**, 78
- Hargrave, P. J., & Ryle, M. 1974, *MNRAS*, **166**, 305
- Hogg, D. W. 1999, ArXiv e-prints [[arXiv:astro-ph/9905116](https://arxiv.org/abs/astro-ph/9905116)]
- Jafry, Y. R., Cornelisse, J., & Reinhard, R. 1994, *ESA Journal*, **18**, 219
- Katz, J. I. 1997, *ApJ*, **478**, 527
- Kikuchi, S., Inoue, M., Mikami, Y., et al. 1988, *A&A*, **190**, L8
- Kokkotas, K. D., & Schmidt, B. G. 1999, *Liv. Rev. Relativ.*, **2**, 72
- Komissarov, S. S. 2009, *J. Korean Phys. Soc.*, **54**, 2503
- Komissarov, S. S., Barkov, M. V., Vlahakis, N., & Königl, A. 2007, *MNRAS*, **380**, 51
- Komossa, S. 2003, in *The Astrophysics of Gravitational Wave Sources*, *AIP Conf. Proc.*, **686**, 161
- Krichbaum, T. P., Roy, A., Lu, R. S., et al. 2014, in *Proc. 12th European VLBI Network Symp. and Users Meeting*, 13
- Kudryavtseva, N. V., Britzen, S., Witzel, A., et al. 2011, *A&A*, **526**, A51
- Kun, E., Frey, S., Gabányi, K.É., et al. 2015, *MNRAS*, **454**, 1290
- Lang, K. R. 2002, *Astrophysical Formulae*, Vol. 2: Space, Time, Matter and Cosmology (Springer)
- Lense, J., & Thirring, H. 1918, *Phys. Z.*, **19**, 156
- Li, Z. Y., Chieuh, Z. H., & Begelman, M. C. 1992, *ApJ*, **394**, 459
- Lister, M. L., Cohen, M. H., Homan, D. C., et al. 2009, *AJ*, **138**, 3718
- Lister, M. L., Aller, M. F., Aller, H. D., et al. 2013, *AJ*, **146**, 120
- Liu, S., & Melia, F. 2002, *ApJ*, **573**, L23
- Lobanov, A. P., & Roland, J. 2005, *A&A*, **431**, 831
- Lu, J. F. 1990, *A&A*, **229**, 424
- Ly, C., Walker, R. C., & Junor, W. 2007, *ApJ*, **660**, 200
- Macdonald, D., & Thorne, K. S. 1982, *MNRAS*, **198**, 345
- Marscher, A. P., & Gear, W. K. 1985, *ApJ*, **298**, 114
- Marscher, A. P., Jorstad, S. G., D'Arcangelo, F. D., et al. 2008, *Nature*, **452**, 966
- McKinney, J. C., Tchekhovskoy, A., & Blandford, R. D. 2012, *MNRAS*, **423**, 2083
- McKinney, J. C., Dai, L. X., & Avara, M. 2015, *MNRAS*, **454**, L6
- Meier, D. L. 1999, *ApJ*, **522**, 753
- Meier, D. L. 2013, *EPJ Web of Conferences*, **61**, 01001
- Merritt, D. 2003, in *Coevolution of Black Holes and Galaxies*, ed. L. C. Ho, 263
- Merritt, D., & Milosavljevic, M. 2005, *Liv. Rev. Relativ.*, **8**, 8
- Milas, D., Katsoulakos, G., Lingri, D., et al. 2014, in *High Energy Phenomena in Relativistic Outflows*, *International Journal of Modern Physics Conference Series*, **28**, 1460200
- Milosavljevic, M., & Merritt, D. 2003, *AIP Conf. Proc.*, **686**, 201
- Misner, C. M., Thorne, K. S., & Wheeler, J. A. 1973, *Gravitation* (San Francisco: Freeman)
- Molina, S. N., Agudo, I., Gomez, J. L., et al. 2014, *A&A*, **566**, A26
- Nakamura, M., & Asada, K. 2013, *ApJ*, **775**, 118
- Narayan, R., McClintock, J. E., & Tchekhovskoy, A. 2014, in *General Relativity, Cosmology and Astrophysics, Fundamental theories of Physics (Proceedings of the Conference, Relativity and Gravitation: 100 Years after Einstein)*, Vol. 177 (Switzerland: Springer International Publishing), 523
- Nelson, R. P., & Papaloizou, J. C. B. 2000, *MNRAS*, **315**, 570
- Nixon, C., & King, A. 2013, *ApJ*, **765**, L7
- Pen, Ue-Li. 1999, *ApJS*, **120**, 49
- Perley, R. A., Dreher, J. W., & Cowan, J. J. 1984, *ApJ*, **285**, L35
- Peters, P. C. 1964, *Phys. Rev.*, **136**, 1224
- Piner, B. G., Pushkarev, A. B., Kovalev, Y. Y., et al. 2012, *ApJ*, **758**, 84
- Priedhorsky, W. C., & Holt, S. S. 1987, *Space Sci. Rev.*, **45**, 291
- Punsly, B. 2001, *Black Hole Gravitohydrodynamics* (New York: Springer)
- Punsly, B., & Coroniti, F. V. 1990, *ApJ*, **350**, 518
- Puschell, J. J., Stein, W. A., Jones, T. W., et al. 1979, *ApJ*, **227**, L11
- Qian, S. J. 1996a, *Chin. Astron. Astrophys.*, **20**, 137
- Qian, S. J. 1996b, *Chin. Astron. Astrophys.*, **20**, 281
- Qian, S. J. 2011, *Res. Astron. Astrophys.*, **11**, 43
- Qian, S. J. 2012, *Res. Astron. Astrophys.*, **12**, 46
- Qian, S. J. 2013, *Res. Astron. Astrophys.*, **13**, 783
- Qian, S. J. 2015, *Res. Astron. Astrophys.*, **15**, 287
- Qian, S. J. 2016, *Res. Astron. Astrophys.*, **16**, 20
- Qian, S. J., Witzel, A., Krichbaum, T., et al. 1991, *Acta Astron. Sin.*, **32**, 369 (english translation: in 1992 *Chin. Astro. Astrophys.*, **16**, 137)
- Qian, S. J., Krichbaum, T. P., Zensus, J. A., et al. 1996, *A&A*, **308**, 395
- Qian, S. J., Kudryavtseva, N. A., Britzen, S., et al. 2007, *Chin. J. Astron. Astrophys.*, **7**, 364
- Qian, S. J., Witzel, A., Zensus, J. A., et al. 2009, *Res. Astron. Astrophys.*, **9**, 137
- Qian, S. J., Krichbaum, T. P., Witzel, A., et al. 2010, *Res. Astron. Astrophys.*, **10**, 47
- Qian, S. J., Britzen, S., Witzel, A., et al. 2014, *Res. Astron. Astrophys.*, **14**, 249
- Raiteri, C. M., Villata, M., Aller, H. D., et al. 2001, *A&A*, **377**, 396
- Roland, J., Britzen, S., Caproni, A., et al. 2013, *A&A*, **557**, A85
- Roland, J., Britzen, S., Kun, E., et al. 2015, *A&A*, **578**, A86
- Romero, G. E., Chajet, L., Abraham, Z., & Fan, J. H. 2000, *A&A*, **360**, 57
- Roos, N., Kaastra, J. S., & Hummel, C. A. 1993, *ApJ*, **409**, 130
- Sarazin, C. L., Begelman, M. C., & Hatchett, S. P. 1980, *ApJ*, **238**, L129
- Savolainen, T., Wiik, K., Valtaoja, E., & Tornikoski, M. 2006, *A&A*, **446**, 71
- Scheuer, P. A. G. 1992, in *Extragalactic Radio Sources: From Beams to Jets*, eds. J. Roland, H. Sol, & G. Pelletier, 368
- Scheuer, P. A. G., & Feiler, R. 1996, *MNRAS*, **282**, 291
- Sesana, A., Vecchio, A., & Volonteri, M. 2009, *MNRAS*, **394**, 2255
- Shakura, N. I., & Sunyaev, R. A. 1973, *A&A*, **24**, 337
- Shapiro, S. L., & Teukolsky, S. A. 1983, *Black Holes, White Dwarfs, and Neutron Stars: the Physics of Compact Objects* (John Wiley & Sons, Inc.)
- Shepherd, M. C. 1997, in *Astronomical Data Analysis Software and Systems VI*, eds. G. Hunt, & H. E. Payne, *ASP Conf. Ser.*, **125**, 77
- Sitko, M. L., Stein, W. A., & Schmidt, G. D. 1984, *ApJ*, **282**, 29
- Sitko, M. L., Schmidt, G. D., & Stein, W. A. 1985, *ApJS*, **59**, 323
- Spergel, D. N., Verde, L., Peiris, H. V., et al. 2003, *ApJS*, **148**, 175
- Steffen, W., Zensus, J. A., Krichbaum, T. P., et al. 1995, *A&A*, **302**, 335
- Stirling, A. M., Cawthorne, T. V., Stevens, J. A., et al. 2003, *MNRAS*, **341**, 405
- Tateyama, C. E. 2009, *ApJ*, **705**, 877
- Tateyama, C. E. 2013, *ApJS*, **205**, 15
- Tateyama, C. E., & Kingham, K. A. 2004, *ApJ*, **608**, 149
- Tchekhovskoy, A., Narayan, R., & McKinney, J. C. 2010, *ApJ*, **711**, 50
- Tchekhovskoy, A., Metzger, B. D., Giannios, D., & Kelley, L. Z. 2014, *MNRAS*, **437**, 2744
- Throne, K. S., & Braginsky, V. B. 1976, *ApJ*, **204**, 11
- Thorne, K. S., & Blandford, R. D. 1982, in *Extragalactic Radio Sources*, eds. D. S. Heeschen, & C. M. Wade (Dordrecht: D. Reidel Publishing), *Proc. Symp.*, **255**
- Tsien, S. C. 1982, *MNRAS*, **200**, 377
- Tsien, S. C., & Saunders, R. 1982, in *Extragalactic Radio Sources* eds. D. S. Heeschen, & C. M. Wade (Dordrecht: D. Reidel Publishing Co.), *Proc. Symp.*, **177**
- Valtonen, M., & Pihajok, P. 2013, *A&A*, **557**, A28
- Valtonen, M., & Wiik, K. 2012, *MNRAS*, **421**, 1861
- Valtonen, M. J., Lehto, H. J., Sillanpää, A., et al. 2006a, *ApJ*, **646**, 36
- Valtonen, M. J., Nilsson, K., Sillanpää, A., et al. 2006b, *ApJ*, **643**, L9
- Valtonen, M. J., Lehto, H. J., Nilsson, K., et al. 2008, *Nature*, **452**, 851
- Valtonen, M. J., Mikkola, S., Merritt, D., et al. 2010, *ApJ*, **705**, 709
- Valtonen, M. J., Lehto, H. J., Takalo, L. O., & Sillanpää, A. 2011, *ApJ*, **729**, 33
- Valtonen, M. J., Zola, S., Ciprini, S., et al. 2016, *ApJ*, **819**, L37
- Villata, M., Raiteri, C. M., Sillanpää, A., & Takalo, L. O. 1998, *MNRAS*, **293**, L13
- Vicente, L., Charlot, P., & Sol, H. 1996, *A&A*, **312**, 727
- Vlahakis, N. 2006, in *Entering the GLAST era*, *APS Conf. Ser.*, **350**, 169
- Vlahakis, N., & Königl, A. 2004, *ApJ*, **605**, 656
- Volonteri, M., Haardt, F., & Madau, P. 2003, *ApJ*, **582**, 559
- Wijnands, R. A. D., Kuulkers, E., & Smale, A. P. 1996, *ApJ*, **473**, L45
- Zamaninasab, M., Clausen-Brown, E., Savolainen, T., & Tchekhovskoy, A. 2014, *Nature*, **510**, 126
- Zhuravlev, V. V., Ivanov, P. B., Fragile, P. C., et al. 2015, *ApJ*, **796**, 104

Appendix A: Additional figures

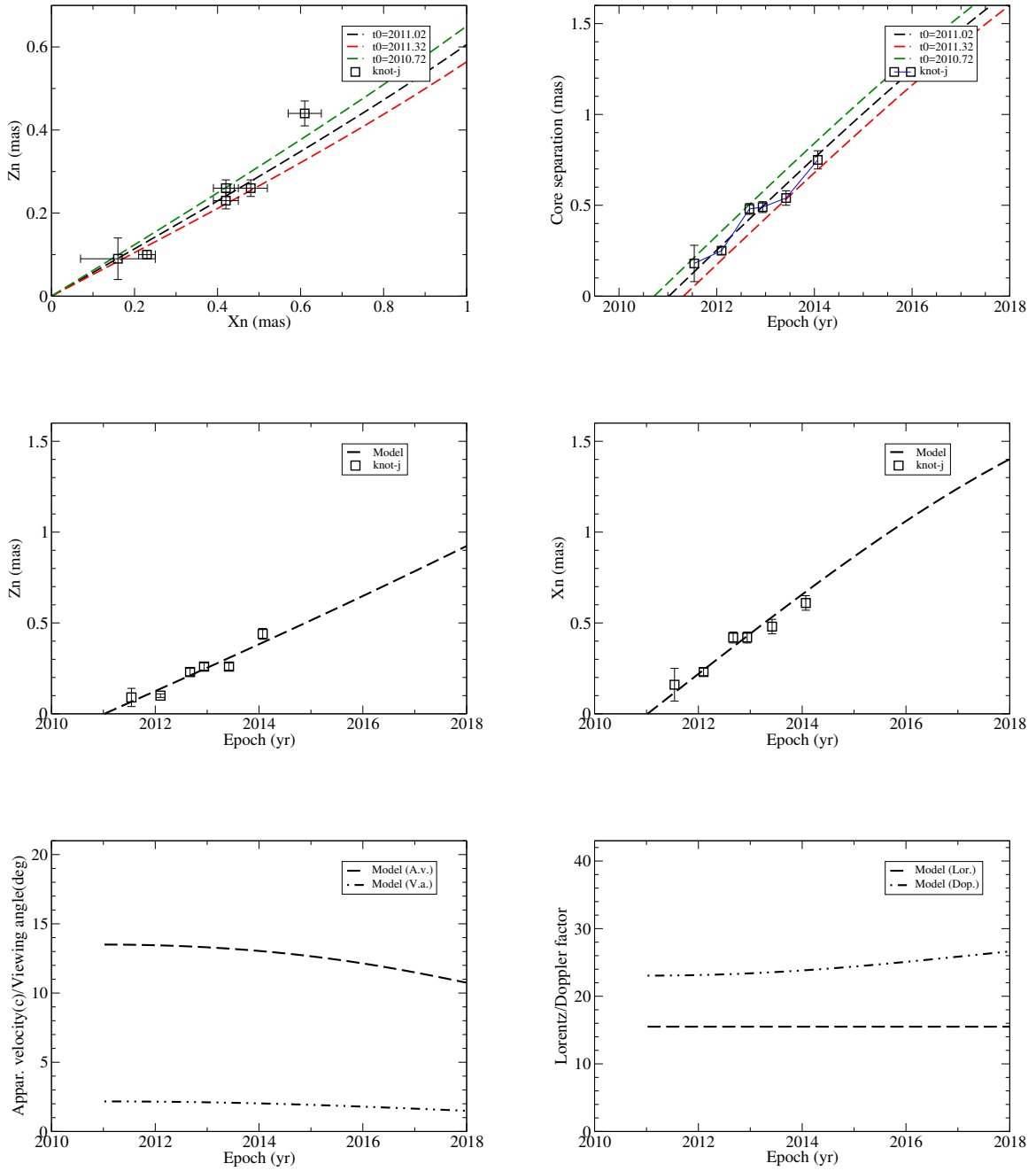


**Fig. A.1.** Model fitting of the kinematics for knot  $j$ : trajectory  $Z_n$ - $X_n$ , core separation  $r_n(t)$ , coordinates  $X_n(t)$  and  $Z_n(t)$ , the modeled apparent velocity/viewing angle and Lorentz/Doppler factor. In each of the *upper plots*, two additional model curves (red and green) are also shown for ejection epochs  $t_0 + 0.3$  yr and  $t_0 - 0.3$  yr ( $t_0 = 2011.02$ ), demonstrating that most of the observational data points are within the regions confined by the two curves and that the precessing period is determined with an uncertainty of  $\sim 0.3$  yr.

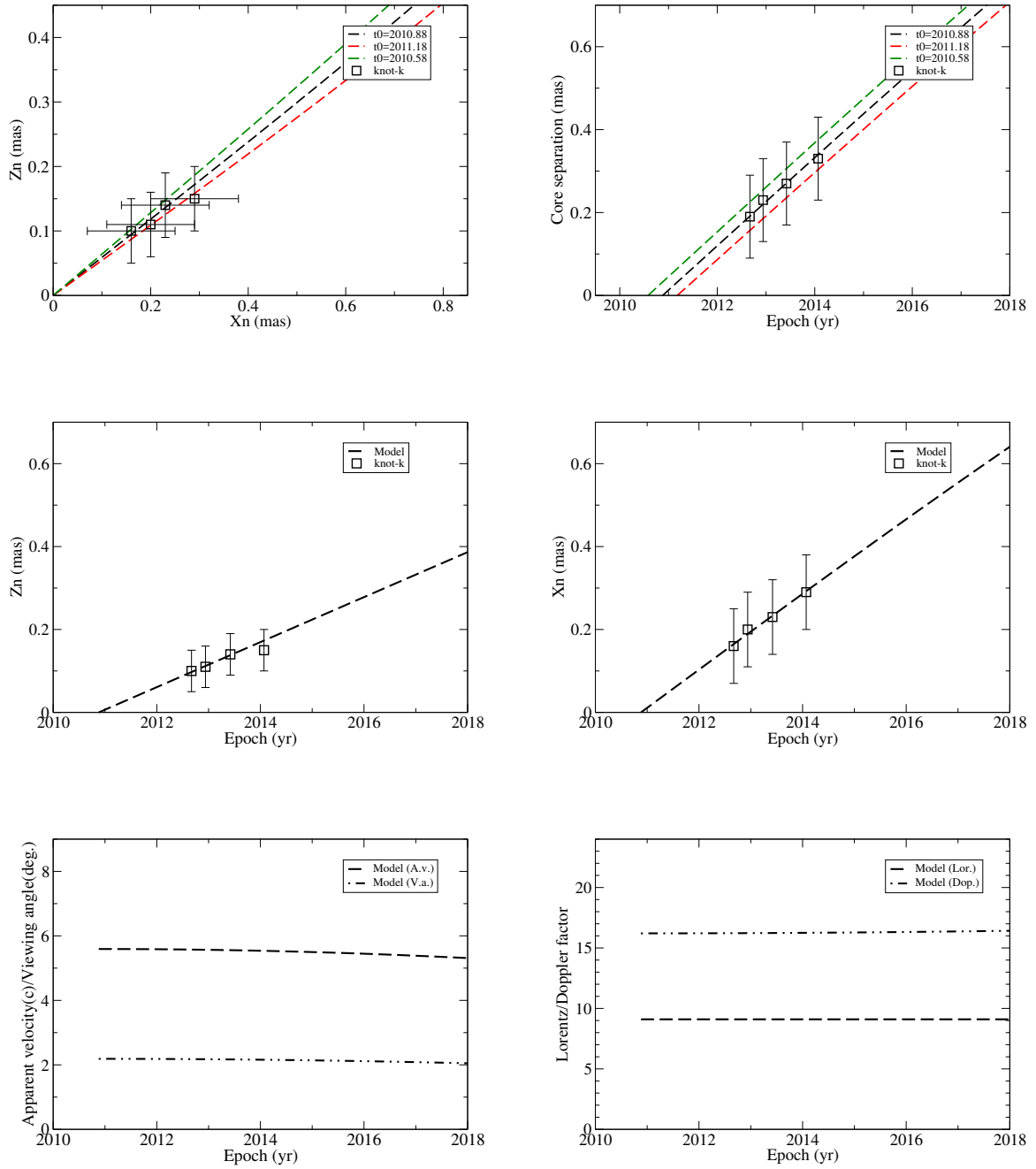


**Fig. A.2.** Model fitting of the kinematics for knot  $k$ : trajectory  $Z_n$ - $X_n$ , core separation  $r_n(t)$ , coordinates  $X_N(t)$  and  $Z_n(t)$ , the modeled apparent velocity/viewing angle and Lorentz/Doppler factor. In each of the *upper plots*, two additional model curves (red and green) are also shown for ejection epochs  $t_0 + 0.3$  yr and  $t_0 - 0.3$  yr ( $t_0 = 2010.88$ ), demonstrating that most of the observational data points are within the regions confined by the two curves and that the precession period is determined with an uncertainty of  $\sim 0.3$  yr.

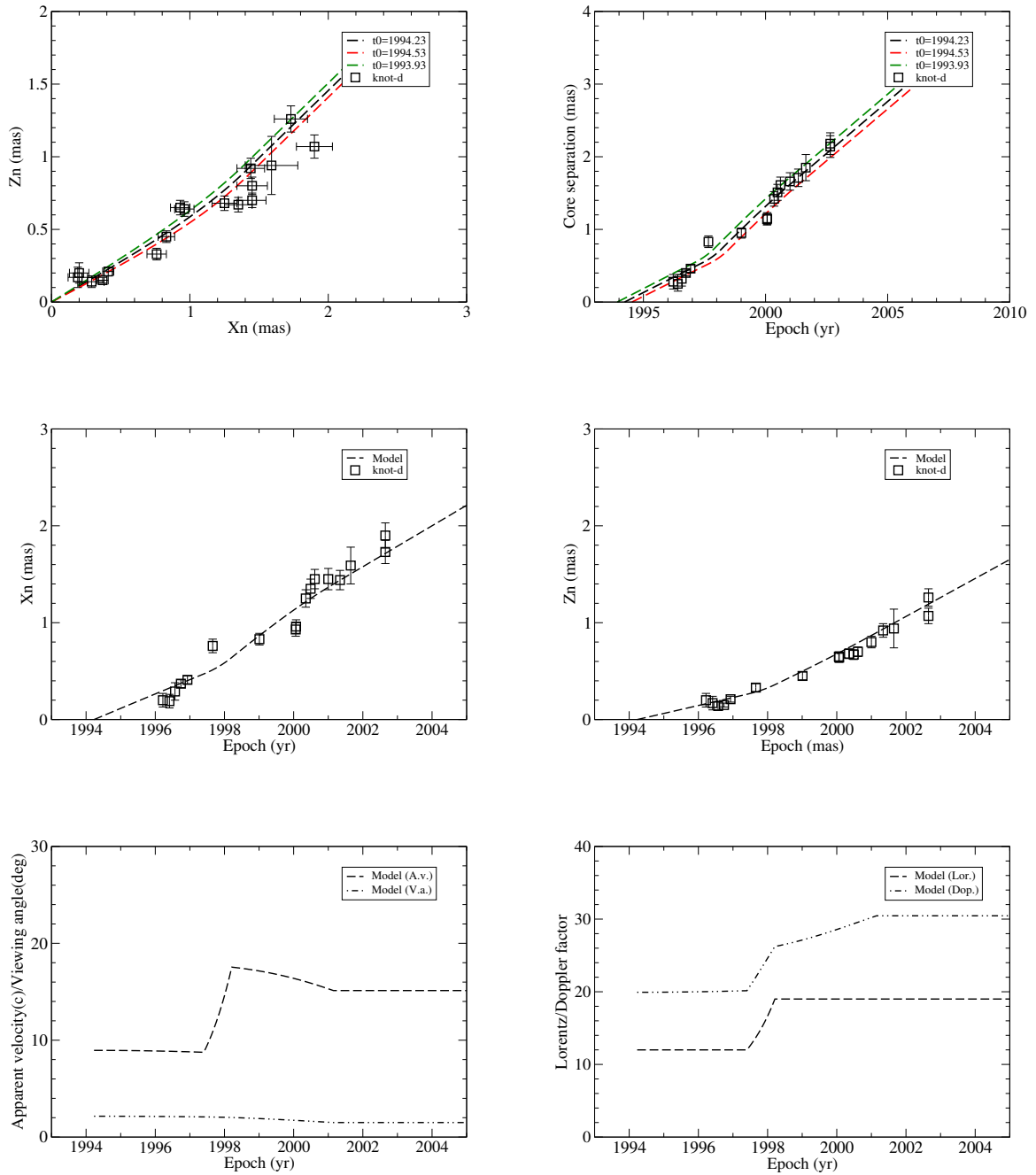


**Fig. A.3.** Model fitting of the kinematics for knot *d*: trajectory  $Z_n$ - $X_n$ , core separation  $r_n(t)$ , coordinates  $X_n(t)$  and  $Z_n(t)$ , the modeled apparent velocity/viewing angle and Lorentz/Doppler factor. The modeled apparent velocity increases from  $\sim 9c$  to  $\sim 17c$ . In each of the *upper plots*, two additional model curves (red and green) are also shown for ejection epochs  $t_0 + 0.3$  yr and  $t_0 - 0.3$  yr ( $t_0 = 1994.23$ ), demonstrating that most of the observational data points are roughly within the regions confined by the two curves and that the precession period is determined with an uncertainty of  $\sim 0.3$  yr.

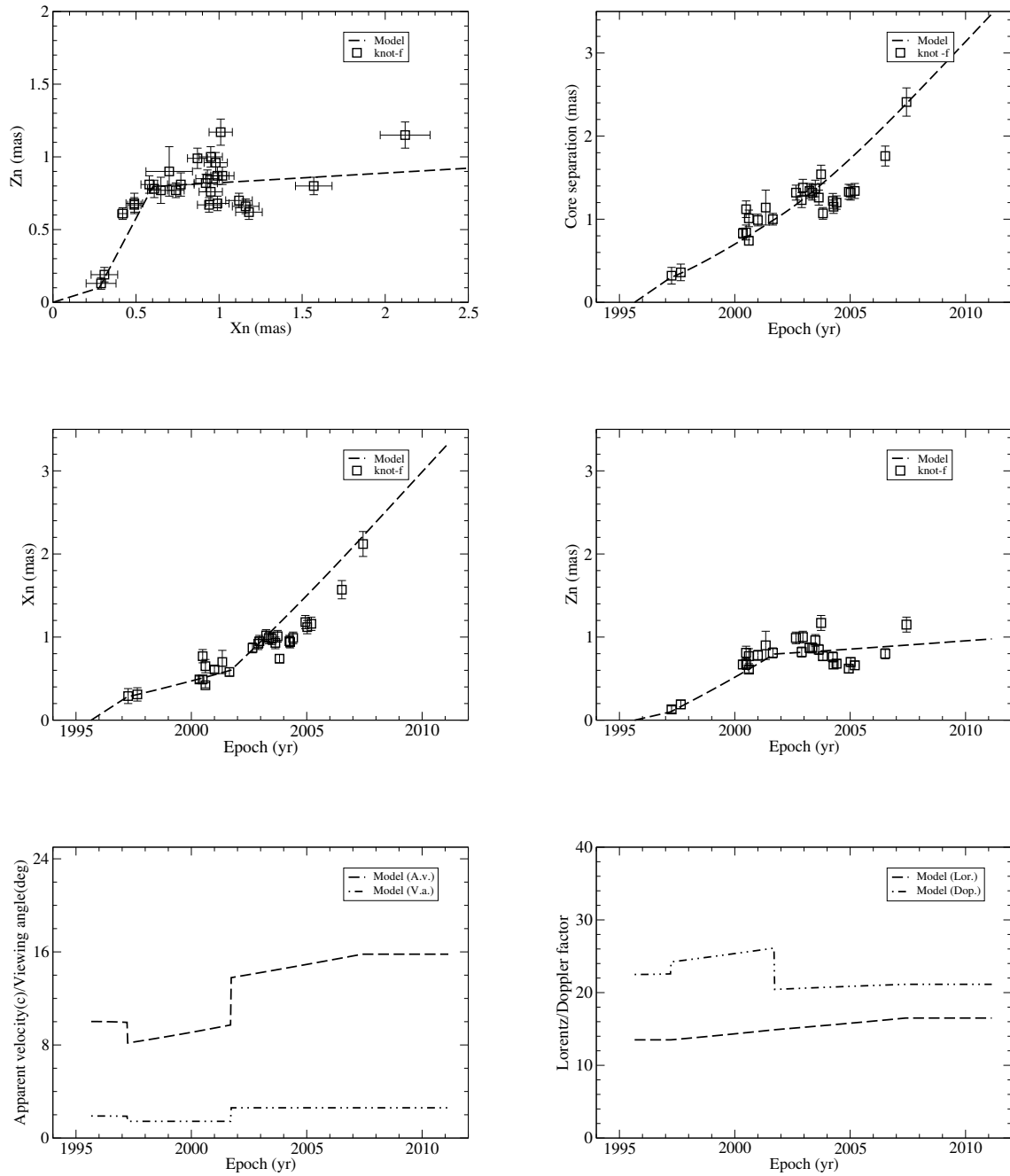


**Fig. A.4.** Model fitting of the kinematics for knot  $f$ : trajectory  $Z_n$ - $X_n$ , core separation  $r_n(t)$ , coordinates  $X_n(t)$  and  $Z_n(t)$ , the modeled apparent velocity/viewing angle and Lorentz/Doppler factor. Its ejection time is assumed to be  $t_0 = 1995.66$  (BQS17). Two curvatures in its trajectory at  $Z = 9$  mas and  $Z = 40$  mas (corresponding to core separations  $r_n = 0.30$  mas and 1.0 mas) are introduced.

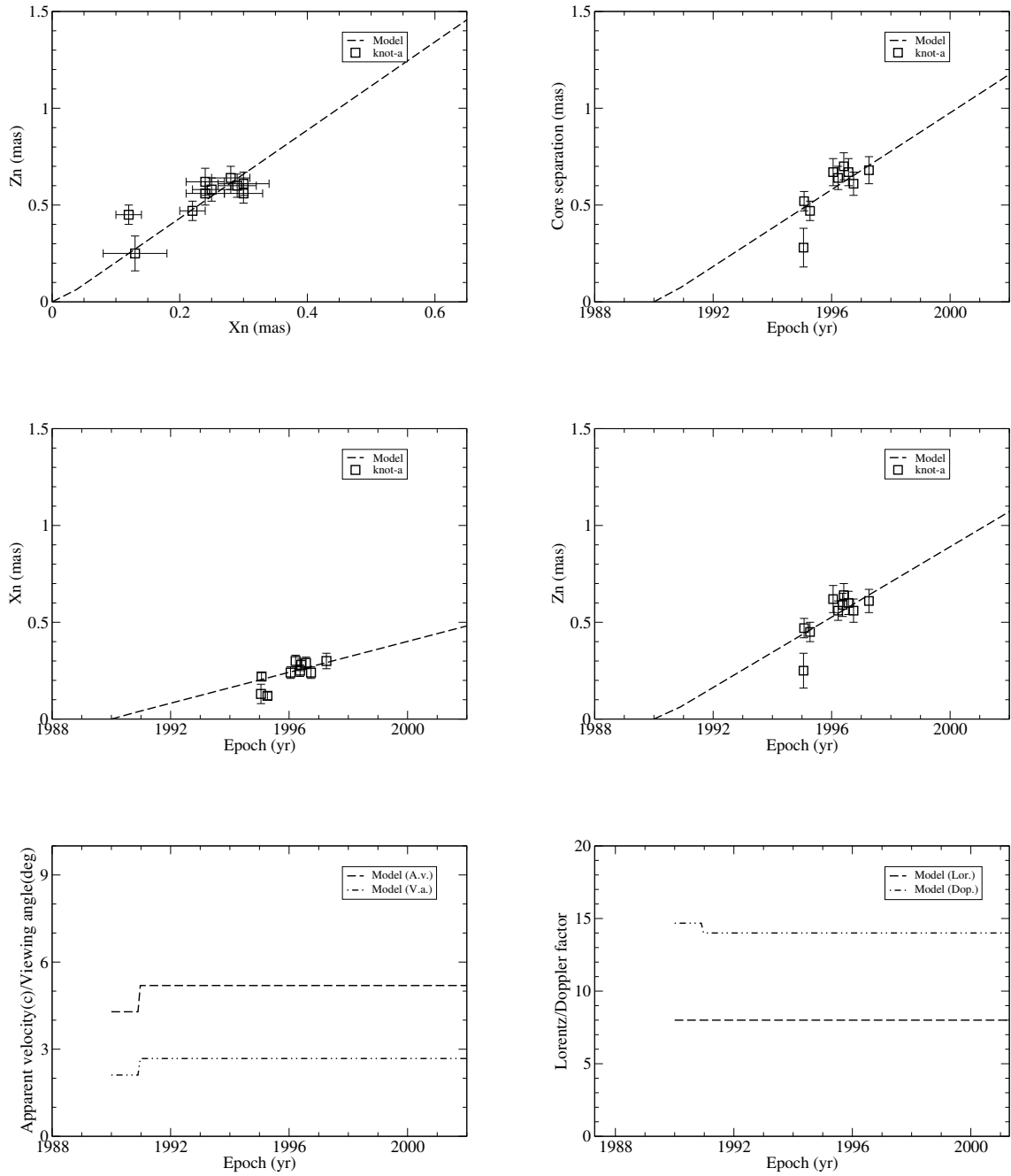


**Fig. A.5.** Model fitting of the kinematics for knot  $a$ : trajectory  $Z_n$ - $X_n$ , separation  $r_n(t)$ , coordinates  $X_n(t)$  and  $Z_n(t)$ , the modeled apparent velocity/viewing angle and Lorentz/Doppler factor. Its ejection time is assumed to be  $t_0 = 1990.0$  (corresponding to a phase  $\phi = 1.77$  rad). A curvature in its trajectory at  $Z = 2.0$  mas (corresponding to a core separation  $r_n = 0.074$  mas) is introduced.

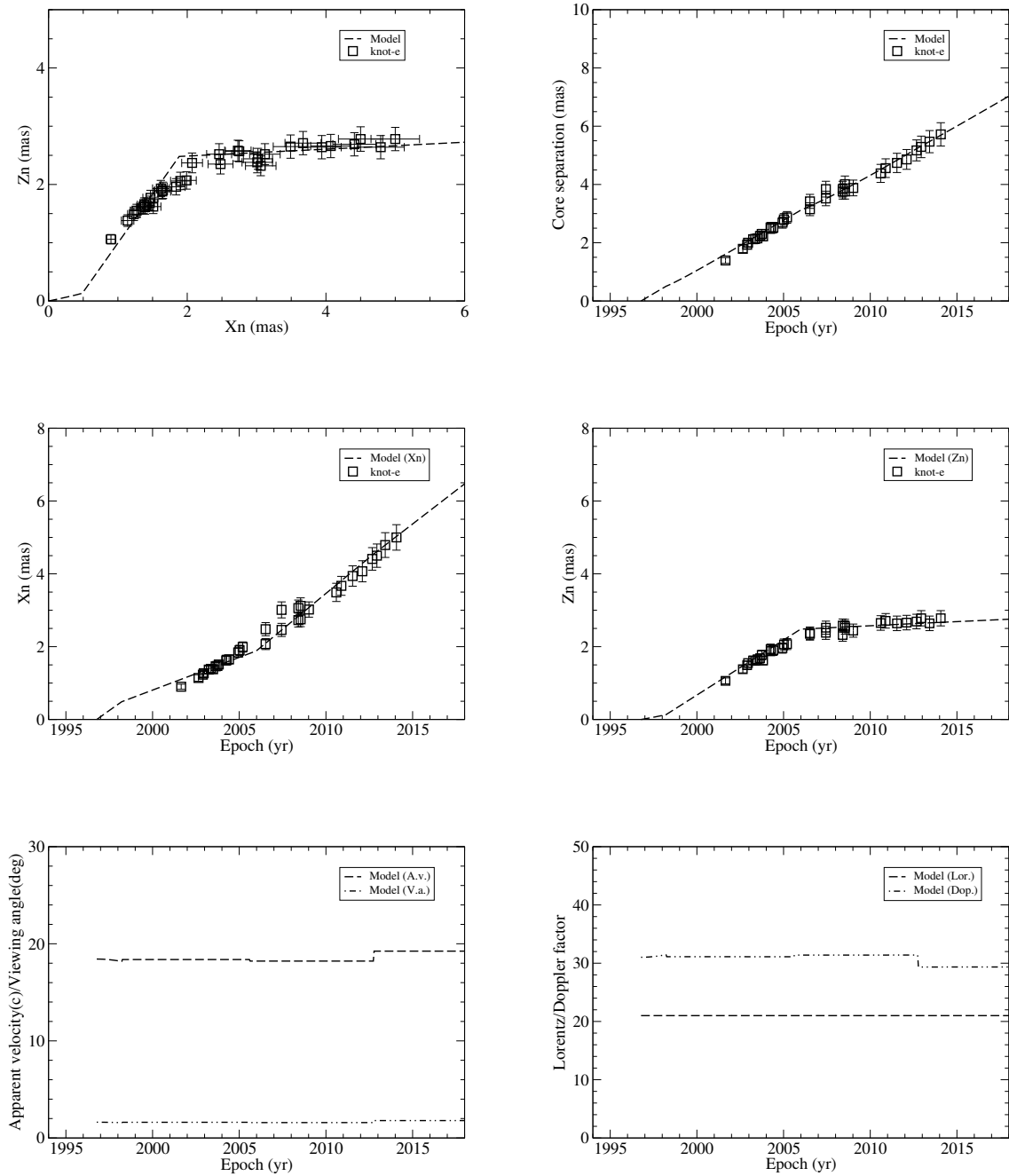


**Fig. A.6.** Model fitting of the kinematics for knot  $e$ : trajectory  $Z_n$ - $X_n$ , core separation  $r_n(t)$ , coordinates  $Z_n(t)$  and  $X_n(t)$ , the modeled apparent velocity/viewing angle and Lorentz/Doppler factor. Its ejection time is assumed to be  $t_0 = 1996.78$  (BQS17). Two curvatures in its trajectory at  $Z = 18$  mas ( $r_n = 0.50$  mas) and  $Z = 115$  mas ( $r_n = 3.1$  mas) are introduced.

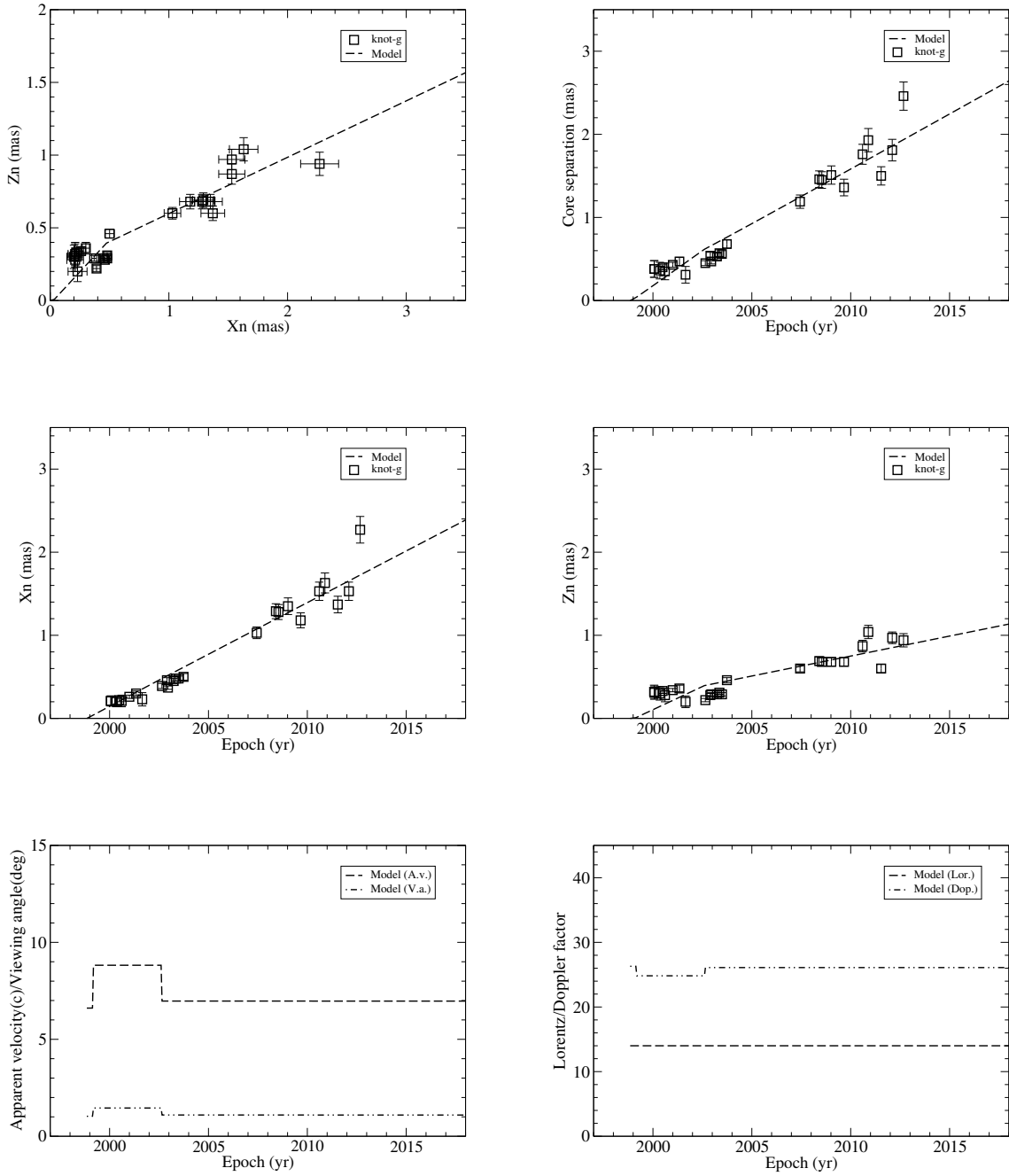


**Fig. A.7.** Model fitting of the kinematics for knot *g*: trajectory  $Z_n$ - $X_n$ , core separation  $r_n(t)$ , coordinates  $X_n(t)$  and  $Z_n(t)$ , the modeled apparent velocity/viewing angle and Lorentz/Doppler factor. Its ejection time is assumed to be  $t_0 = 1998.85$  (BQS17). Two curvatures in its trajectory at  $Z = 2.0$  mas ( $r_n = 0.036$  mas) and  $Z = 25$  mas ( $r_n = 0.62$  mas) are introduced.